



This is a repository copy of *The tectonics of the western Ordos Plateau, Ningxia, China: Slip rates on the Luoshan and East Helanshan Faults.*

White Rose Research Online URL for this paper:
<http://eprints.whiterose.ac.uk/109870/>

Version: Accepted Version

Article:

Middleton, T.A., Walker, R.T., Rood, D.H. et al. (6 more authors) (2016) The tectonics of the western Ordos Plateau, Ningxia, China: Slip rates on the Luoshan and East Helanshan Faults. *Tectonics*, 35 (11). pp. 2754-2777. ISSN 0278-7407

<https://doi.org/10.1002/2016TC004230>

This is the peer reviewed version of the following article: Middleton, T. A. et al (2016), The tectonics of the western Ordos Plateau, Ningxia, China: Slip rates on the Luoshan and East Helanshan Faults, *Tectonics*, 35, 2754–2777, which has been published in final form at <https://doi.org/10.1002/2016TC004230>. This article may be used for non-commercial purposes in accordance with Wiley Terms and Conditions for Self-Archiving.

Reuse

Unless indicated otherwise, fulltext items are protected by copyright with all rights reserved. The copyright exception in section 29 of the Copyright, Designs and Patents Act 1988 allows the making of a single copy solely for the purpose of non-commercial research or private study within the limits of fair dealing. The publisher or other rights-holder may allow further reproduction and re-use of this version - refer to the White Rose Research Online record for this item. Where records identify the publisher as the copyright holder, users can verify any specific terms of use on the publisher's website.

Takedown

If you consider content in White Rose Research Online to be in breach of UK law, please notify us by emailing eprints@whiterose.ac.uk including the URL of the record and the reason for the withdrawal request.



eprints@whiterose.ac.uk
<https://eprints.whiterose.ac.uk/>

1 The tectonics of the western Ordos Plateau, Ningxia,
2 China: slip rates on the Luoshan and East Helanshan
3 Faults

Timothy A. Middleton,¹ Richard T. Walker,¹ Dylan H. Rood,² Edward J.

Rhodes,³ Barry Parsons,¹ Qiyun Lei,⁴ Yu Zhou,¹ John R. Elliott,¹ and

Zhikun Ren⁵

Authors' manuscript, submitted version of paper published as:
Tectonics, 35, 2754–2777, doi:10.1002/2016TC004230

Key Points.

- Here is the first keypoint. what happens
if it is a long keypoint, like this one. We
want to see this wrap please.
- This is the second.
- And here is the third keypoint

Corresponding author: Timothy A. Middleton, COMET, Department of Earth Sciences, University of Oxford, South Parks Road, Oxford, OX1 3AN, UK. (tim.middleton@earth.ox.ac.uk)

¹COMET, Department of Earth Sciences,

4 **Abstract.**

5 Analysis of the locus, style and rates of fault-
6 ing is fundamental to understanding the kine-
7 matics of continental deformation. The Or-
8 dos Plateau lies to the northeast of Tibet, within
9 the India-Eurasia collision zone. Previous stud-

University of Oxford, South Parks Road,
Oxford, OX1 3AN, UK

²Department of Earth Science and
Engineering, Imperial College London,
South Kensington Campus, London SW7
2AZ, UK & AMS Laboratory, Scottish
Universities Environmental Research
Centre, East Kilbride G75 0QF, UK

³Department of Geography, University of
Sheffield, Sheffield, S10 2TN, UK

⁴Ningxia Seismological Bureau, Yinchuan,
China

⁵State Key Laboratory for Earthquake
Dynamics, Institute of Geology, China
Earthquake Administration, Beijing, China

ies have suggested that it behaves rigidly and
rotates anticlockwise within a large-scale zone
of ENE-WSW left-lateral shearing. For this
rotation to be accommodated, the eastern and
western margins of the Ordos Plateau should
be undergoing right-lateral shearing and yet
the dominant faulting style appears to be ex-
tensional. We focus specifically on the kine-
matics of the faults bounding the western mar-
gin of the Ordos Plateau and make new slip
rate estimates for two of the major faults in
the region: the right-lateral strike-slip Luoshan
Fault and the normal-slip East Helanshan Fault.
We use a combination of IRSL dating of off-
set landforms with high-resolution imagery and
topography from the Pleiades satellites to de-
termine an average right-lateral slip rate of 4.3 ± 0.4 mm/a
(1σ uncertainties) on the Luoshan Fault. Sim-
ilarly, we use ^{10}Be exposure dating to deter-
mine a throw rate on the East Helanshan Fault
of 0.8 ± 0.1 mm/a, corresponding to an exten-
sion rate of 0.9 ± 0.1 mm/a (1σ uncertainties).

32 We therefore conclude that right-lateral shear-
33 ing is the dominant motion occurring in the
34 western Ordos region, supporting a kinematic
35 model of large-scale anticlockwise rotation of
36 the whole Ordos Plateau.

1. Introduction

37 Deformation on the continents tends to be distributed across broad networks of faults
38 (e.g. *Thatcher* [2009]). For instance, in the India-Eurasia collision zone, 4 cm/a of
39 relative motion is accommodated in a region spanning thousands of kilometres [*DeMets*
40 *et al.*, 1990, 1994; *England and Molnar*, 1997; *Wang et al.*, 2001]. Within the India-
41 Eurasia collision zone, though, there are also regions that appear not to deform. It
42 is important to understand the active tectonics of such regions because non-deforming
43 blocks tend to localise strain, and hence seismic hazard, at their margins (e.g. *Molnar and*
44 *Dayem* [2010]), yet the style of faulting and rates of motion of these blocks are not always
45 predictable from nearby plate velocities (e.g. *McKenzie and Jackson* [1983]; *Jackson*
46 *and McKenzie* [1988]). For example, large-scale transtensional shearing can sometimes
47 be accommodated purely by en-echelon normal faulting and vertical axis rotations of
48 intervening crustal blocks [*Wesnowsky et al.*, 2012].

49 The Ordos Plateau, which lies to the northeast of the Tibetan Plateau in northern
50 central China, is one such apparently non-deforming region. It sits within the India-
51 Eurasia collision zone—hence in a region of overall shortening—and yet large normal
52 faults and extensional grabens are present along most of its boundaries, suggesting that
53 the region is extending in all directions (see Figure 1). However, both geological and
54 GPS measurements indicate that the Ordos Plateau is situated within a large, left-lateral
55 shear zone and should be rotating anticlockwise about a vertical axis within this zone,
56 indicating predominantly strike-slip motion at its edges [*Xu and Ma*, 1992; *Xu et al.*,
57 1993; *Avouac and Tapponnier*, 1993; *Xu et al.*, 1994; *Zhang et al.*, 1995; *Peltzer and*

58 *Saucier, 1996; Zhang et al., 1998; Zhao et al., 2015*] (see Figures 2 (a), 1 (b) and 1 (c)).
59 Yet evidence for anticlockwise rotation of the Ordos Plateau is relatively sparse. *Xu*
60 *et al.* [1994] used palaeomagnetic data to estimate a total anticlockwise rotation of 1.3
61 to 3.7° with respect to the Xinjiang region of northwest China since the Late Tertiary,
62 corresponding to a rotation rate of 0.5 to $1.4^\circ/\text{Ma}$. However, their samples are from the
63 deforming eastern margin of the Ordos Plateau (see Figure 1), and so are likely to be
64 affected by local rotations within this deforming belt. Furthermore, *Li et al.* [2001] report
65 much higher anticlockwise rotation rates of tens of degrees per million years, also on the
66 basis of palaeomagnetic data (see Figure 1)—although their samples are also primarily
67 from the deforming margins of the Ordos Plateau. *Fan and Ma* [2003] used the fairly
68 sparse GPS dataset of *Wang et al.* [2001] (including only 6 sites on the Ordos Plateau)
69 to estimate an anticlockwise rotation rate of $0.02^\circ/\text{Ma}$ about a pole at 51.5°N , 120.1°E
70 with respect to stable Eurasia.

71 If anticlockwise rotation about a vertical axis is important for the kinematics of the
72 Ordos Plateau, we would expect to see dominantly right-lateral motion on both the eastern
73 and western sides of the plateau as it rotates with respect to the Alxa Desert in the west
74 and the North China Plain in the east (see Figure 1). On the eastern side of the Ordos
75 Plateau it is known that right-lateral shearing occurs through normal faulting on the en-
76 echelon Shanxi Grabens and right-lateral slip on the Xizhoushan Fault (at 5.7 mm/a) and
77 the Huoshan Fault (at 7 mm/a) [*Xu et al., 1986; Xu and Deng, 1990*] (see later Figure 19
78 for locations). On the western side of the Ordos Plateau, right-lateral faults are also

79 identified, though their rates of motion and relative importance are debated (e.g. *Deng*
80 *et al.* [1984]; *Min et al.* [1992, 1993]; *Zhang et al.* [1998]; *Min et al.* [2003]).

81 In this study we therefore examine the relative importance of right-lateral and exten-
82 sional slip in the western Ordos region by determining Holocene rates for two of the
83 major faults within the region: the Luoshan Fault (right-lateral strike-slip) and the East
84 Helanshan Fault (normal). We then use our results to build a kinematic model of the
85 Ordos Plateau that incorporates both anticlockwise rotation and the widespread normal
86 faulting.

2. Tectonic setting

87 The western Ordos region straddles the transition from the shortening occurring in the
88 northeastern corner of the Tibetan Plateau to the apparent extension occurring across
89 the Yinchuan Graben. Many recent studies have indicated that deformation in northeast
90 Tibet has accelerated since about 15 Ma ago and that the orientation of the regional stress
91 field has changed since about 20 Ma ago (e.g. *Molnar and Stock* [2009]; *Yuan et al.* [2013]
92 and references therein). Within the western Ordos region, apatite fission track dating
93 reveals rapid uplift and exhumation of the Helanshan 10-12 Ma ago [*Liu et al.*, 2010] and
94 the Liupanshan around 8 Ma ago [*Zheng et al.*, 2006] (see Figure 1). It seems likely that
95 motions at the margins of the Ordos Plateau are sensitive to changes in the stress field in
96 northeast Tibet and were initiated at a similar time (e.g. *Wang et al.* [2013]; *Chen et al.*
97 [2015]).

98 Four large, historical earthquakes have occurred in the vicinity (see Figure 3): the 1561
99 M 7.3 earthquake near the Luoshan Fault [*Min et al.*, 2003]; the 1709 M 7.3 oblique

100 left-lateral strike-slip-faulting Zhongwei earthquake [*Nie and Lin*, 1993; *Min et al.*, 2001];
101 the 1739 M 7.6 normal-faulting Yinchuan earthquake [*Liao and Pan*, 1982; *Zhang et al.*,
102 1986; *Deng and Liao*, 1996; *Bai and Jiao*, 2005; *Chai et al.*, 2006; *Lin et al.*, 2013; *Lei*
103 *et al.*, 2015; *Lin et al.*, 2015; *Middleton et al.*, 2015]; and the 1920 M 8.5 left-lateral strike-
104 slip-faulting Haiyuan earthquake [*Zhang et al.*, 1987, 1988; *Burchfiel et al.*, 1991; *Lasserre*
105 *et al.*, 2002; *Liu-Zeng et al.*, 2007; *Ren et al.*, 2015].

106 The left-lateral Haiyuan Fault, with a Quaternary slip rate in the range of 5 to 10 mm/a
107 [*Zhang et al.*, 1990; *Min et al.*, 2000; *Li et al.*, 2009], runs along the northeastern edge of
108 the Tibetan Plateau and enters the southern part of Ningxia Province, on the western side
109 of the Ordos Plateau, striking northwest-southeast and terminating in a series of reverse
110 faults. These reverse faults form a south-trending fold-and-thrust zone that extends as
111 far as the Liupanshan at the southernmost extent of the province [*Deng et al.*, 1984; *Li*
112 *et al.*, 2013]. The M 8.5 1920 earthquake occurred on the easternmost part of the Haiyuan
113 Fault [*Zhang et al.*, 1987; *Ren et al.*, 2015].

114 To the north of the Haiyuan Fault are three more sets of oblique reverse faults: the
115 Tianjinshan-Miboshan Fault (also called the Zhongwei-Tongxin Fault), the Yantongshan
116 Fault, and the Niushoushan and Luoshan Faults (see Figure 3). The existence and orienta-
117 tion of these ranges implies northeast-southwest crustal shortening, which is in agreement
118 with modern GPS studies [*Gan et al.*, 2007; *Li et al.*, 2013]. The M 7.3 1709 Zhongwei
119 earthquake is thought to have occurred on the Tianjinshan-Miboshan Fault.

120 The two faults that we examine in detail in this paper—the Luoshan right-lateral strike-
121 slip fault and the East Helanshan normal fault—are discussed separately in Sections 4 and
122 5.

3. Methods

3.1. Pleiades data and DEM construction

123 We acquired Pleiades stereo imagery of the central portion of the Luoshan Fault (on
124 18th July 2014) and the southern portion of the East Helanshan Fault (on 23rd April and
125 17th July 2014). See Figure 3 for data coverage. We then constructed high-resolution
126 digital elevation models (DEMs) of each region according to the methodology outlined in
127 *Middleton et al.* [2015] and *Zhou et al.* [2015] (see also Supporting Information).

128 The resulting DEM for the Luoshan Fault has a horizontal resolution of 1 to 2 m (48%
129 of 1 m by 1 m grid cells contain at least one point, whilst 74% of 2 m by 2 m grid
130 cells contain at least one point). A surface roughness map was calculated from the DEM
131 by finding the standard deviation of the slope in a 9×9 m moving window [*Frankel and*
132 *Dolan, 2007*]. The resulting DEM for the southern end of the East Helanshan Fault has
133 a horizontal resolution, at least around the scarps, of about 2 m [*Middleton et al., 2015*].
134 Again, a surface roughness map was calculated, this time using a 5×5 m moving window
135 as this window size was found to more clearly highlight the roughness contrast between
136 different geomorphological surfaces [*Frankel and Dolan, 2007*].

137 For each region, we used the DEM in combination with the surface roughness data
138 and the original imagery to map the fault scarps and geomorphology in detail, tying our
139 remote sensing observations to our field investigations. For the southern end of the East

140 Helanshan Fault, we also calculated the 5th, 25th, 50th, 75th and 95th percentiles of the
141 surface roughness raster for each of the mapped geomorphological units. The median
142 roughness values show an initial decrease with age, followed by a slight increase for the
143 oldest terrace. This agrees with the results of *Frankel and Dolan* [2007]: the initial bar
144 and swale topography on the fan surface is smoothed over time by erosion, but eventually
145 the surface is made rougher again by channel incision. All DEMs, surface roughness data
146 and geomorphological maps are shown in later figures in the results sections.

3.2. Offset measurements

147 We measured vertical offsets across fault traces by drawing swath profiles across the
148 raw point cloud data and fitting lines above and below the scarp. The quoted errors on
149 our vertical offset measurements refer to the root mean square (RMS) residuals from this
150 line fitting process. We determined horizontal offsets from the original Pleiades imagery
151 by fitting straight lines (by eye) to offset geomorphological markers. We then measured
152 the horizontal distance between the two piercing points, where these lines intersected
153 our mapped fault trace. Unless otherwise stated, quoted errors on our horizontal offset
154 measurements are 1σ standard deviations based on suites of measurements from sets
155 of geomorphological features that appear to have been displaced by the same amount
156 (according to our field observations). Full details of our methodologies are given in the
157 Supporting Information and horizontal offset measurements are recorded in Table 1.

3.3. Quaternary dating of offset features

158 On the Luoshan Fault the fluvial sediments contained abundant silts and fine sand
159 horizons, so we used infrared stimulated luminescence (IRSL) dating to constrain the ages

160 of offset geomorphological features (unfortunately, radiocarbon dating was not possible
161 due to the absence of datable material). Full details of the dating technique and sample
162 preparation procedure are given in the Supporting Information, and the results are shown
163 in Table 2. The quoted errors refer to 1σ analytical uncertainties propagated in quadrature
164 unless otherwise stated.

165 On the East Helanshan Fault the alluvial fans comprise poorly consolidated, sub-angular
166 gravels, pebbles, cobbles and boulders, with very little vegetation. The coarse grain size
167 and lack of preserved organic material precluded dating by either radiocarbon or IRSL
168 methods (with the exception of a few very recent deposits, which are well-exposed in
169 modern river channels—see *Middleton et al.* [2015]). We therefore used ^{10}Be exposure
170 dating of boulder tops and suites of quartz pebbles to provide age constraints on the East
171 Helanshan Fault. Background to the ^{10}Be dating procedure and details of the sample
172 preparation and analysis are included in the Supporting Information. The results are
173 given in Table 4.

174 Again, the quoted errors refer to 1σ analytical uncertainties propagated in quadrature
175 unless otherwise stated. A number of our ^{10}Be ages are from amalgamated samples and
176 in these cases we do not have any constraints on the spread of ages within the population
177 of sampled clasts. It should be emphasised, therefore, that the errors on the amalgamated
178 samples still refer to analytical uncertainties and not the standard deviations within the
179 populations.

180 In order to calculate errors on our slip rate estimates we propagate fractional uncertain-
181 ties from our offset measurements and our age results in quadrature. On the strike-slip

182 Luoshan Fault we report horizontal slip rates, whereas on the normal East Helanshan
183 Fault we initially report throw rates because we do not have good constraints on the
184 fault dip. However, on the northern, strike-slip section of the East Helanshan Fault (see
185 Section 5.5) we again report horizontal slip rates.

4. The Luoshan Fault

4.1. Background

186 The Luoshan Fault is approximately 60 km long and runs along the eastern side of
187 the Luoshan (Luo Mountains) [*Min et al.*, 2003]. The Luoshan comprise two ranges: the
188 Daluoshan (Big Luo Mountains) to the north and the Xiaoluoshan (Small Luo Mountains)
189 to the south, both of which are composed of Ordovician basement (see Figure 4). The
190 Luoshan Fault was originally thought to be a left-lateral strike-slip fault [*The Research*
191 *Group on "Active Fault System around Ordos Massif"*, 1988; *Zhang et al.*, 1990; *Zhou*
192 *et al.*, 2000], but a detailed re-assessment found numerous examples of right-lateral offsets
193 in Quaternary and Holocene material [*Min et al.*, 1992, 1993, 2003]. Evidence for recent,
194 right-lateral motion is also seen further south on the Yunwushan Fault in the form of
195 displaced river channels (for example at 36.635 °N, 106.349 °E and 36.531 °N, 106.333 °E—
196 see Figure 3). *Min et al.* [2003] used two thermoluminescence (TL) ages to estimate
197 a minimum, right-lateral slip rate on the Luoshan Fault since the Late Pleistocene of
198 2.15 ± 0.20 mm/a. The fault is assigned a right-lateral rate of 3 mm/a on the *Map of*
199 *Active Tectonics in China* [*Deng et al.*, 2004]. *Min et al.* [2003] also suggest that the
200 1561 M 7.3 earthquake occurred on the Luoshan Fault (see Figure 3) on the basis that
201 comparatively young-looking gullies (1 m deep) record offsets of 1.5 to 5.4 m and that a

202 free face is visible on some scarps, particularly near the village of Zhangjiashanpo (see
203 Figure 4 (a) for location). Given the uncertainty about the kinematics of the Luoshan
204 Fault and the paucity of slip rate constraints, we re-visit the fault in this study using
205 up-to-date luminescence methods and modern satellite imagery.

206 At its northern end, the Luoshan Fault strikes at 353° and runs along the eastern side
207 of the Luoshan mountains just west of Tanzhuangzicun (see Figure 4). Gullies draining
208 these mountains dissect an alluvial apron, draining first to the east and then curving to the
209 north to follow the local slope, and preserve evidence of right-lateral offsets. Moving south,
210 the fault strike changes to 330° around the northern end of the Daluoshan. Surface offsets
211 are harder to identify, but *Min et al.* [2003] found evidence of thrusting in this section.
212 The fault then tracks south, with a strike of 358° , cutting across at least four different
213 generations of alluvial fans (F1-4, where F1 is the youngest and F4 is the oldest) emanating
214 from the Daluoshan (see Figures 5 (a) and 5 (b)). The older fans are more heavily incised
215 and the channels on these surfaces are more sinuous. The different generations of alluvial
216 fans are evident on slope and roughness maps (see later Figures 9 (a) and 9 (b)). Multiple,
217 parallel scarps are seen in this section, most of which include a component of uplift on
218 their western side; the youngest fans preserve a vertical offset of 1.1 ± 0.3 m (see Figure 5
219 (b)). At the southern end of the Daluoshan section, the fault makes a small dog-leg to the
220 southeast and forms a 5 to 10 m high, 500 m long pressure ridge at 37.240°N , 106.322°E .

221 Moving south again, the fault lies along the eastern side of the Xiaoluoshan with a strike
222 of 342° . It cuts across the heads of a number of alluvial fans, most of which appear to be of
223 the same age on the basis of their colour and texture (for example, see Figures 5 (c) and 5

(d)). The streams draining the Xiaoluoshan preserve a number of examples of right-lateral offsets and the fans here are uplifted on the eastern side of the fault trace by 5.0 ± 1.4 m (see Figure 5 (d)). The fault then continues in this orientation until the southern end of the Xiaoluoshan, 9 km south of Zhangjiashanpo. In addition, a series of 12 to 23 m high east-facing scarps are present east of the main strike-slip fault, between 106.34°E and 106.39°E (see Figure 4 (a)). We interpret these scarps to represent superficial spatial separation of strike-slip and reverse components of motion onto two parallel fault strands.

The smallest vertical offset (1.1 ± 0.3 m), at 37.255°N , 106.320°E , was measured where the local fault strike is 003° (see Figure 5 (b)). Other sections of the fault, with more northwesterly strikes, showed larger vertical offsets indicating a greater amount of shortening. We therefore deduce that pure strike-slip motion occurs at an azimuth slightly east of 003° .

Slip rate sites at Xiaoluoshan, Tanzhuangzicun, Shiyadong and Machanggou are described separately below.

4.2. Xiaoluoshan section

4.2.1. Overview and offset measurement

Our first slip rate site on the Luoshan Fault is adjacent to the Xiaoluoshan (see Figure 4 (a)). Here, the fault cuts through an alluvial apron on the eastern side of the mountains and a large number of channels (approximately 300 m spacing) flow eastwards across the fault trace, draining the Xiaoluoshan. Almost all of these channels show evidence of tens of metres of right-lateral offset. There is also a small amount of uplift (approximately 5 m) on the eastern side of the fault trace (see Figure 5 (d)).

245 Given that the whole area appears to be covered by an alluvial apron composed of
246 coalesced fans of the same age, we propose that all of the geomorphological markers should
247 preserve the same offset. We measured the offsets preserved by nine different markers (six
248 channel riser tops, one channel riser bottom and two channel thalwegs—see yellow lines in
249 Figure 6 (b)) according to the methodology described in the Supporting Information and
250 obtained a mean offset of 37.2 ± 5.5 m and range of 29.2 to 44.4 m (see Table 1). Figures 6
251 (c) and 6 (d) show that a 37 m restoration aligns an indistinct riser on the western side of
252 the fault trace with a more pronounced channel margin (from which IRSL sample 2 was
253 taken) on the uplifted eastern side. At the site of IRSL sample 1, the right-lateral fault
254 motion is superposed on a pre-existing channel meander so the horizontal offset is harder
255 to determine. However, Figures 6 (e) and 6 (f) show that the 37 m restoration aligns both
256 a channel thalweg to the south of the sampling site and a ridge crest adjacent to the site.

257 **4.2.2. Age constraints and slip rate**

258 IRSL sample 2 was taken from a channel riser on the eastern side of the fault at
259 37.178°N , 106.340°E . The sample was from a patch of slightly coarser sand interbed-
260 ded with fine-grained, brown loess at a depth of 55 cm. An angular gravel layer with
261 10 cm clasts is visible approximately 30 cm above the sample (see Figure 7 (b)), ensuring
262 that we are dating material that was deposited prior to or during a fluvial regime, rather
263 than aeolian deposits that have accumulated after fan abandonment. The IRSL sample
264 returned an age of 9.2 ± 0.6 ka (see Table 2).

265 IRSL sample 1 was taken from the same alluvial surface, 930 m to the northwest of IRSL
266 sample 2, at 37.185°N , 106.335°E . The sample was taken from a fine-grained, brown loess

267 1.5 m below the ground surface. However, due to erosion at the site, this was estimated
268 in the field to correspond to 2.1 m below the top of the adjacent alluvial fan. The sample
269 was overlain by a coarser sand layer and at least two gravel layers with 5 cm, sub-angular
270 clasts of dark, Palaeozoic bedrock (see Figure 6 (d)). The sample returned an age of
271 141 ± 12 ka (see Table 2).

272 The mean offset (37 m) and the age of IRSL sample 2 allow us to calculate a minimum
273 slip rate of 4.1 ± 0.7 mm/a (see Table 3). Meanwhile, IRSL sample 1 indicates a minimum
274 slip rate of 0.26 ± 0.05 mm/a (see Table 3). IRSL sample 1 is from deeper in the stratig-
275 raphy than IRSL sample 2, and may therefore represent sediments from a period of fan
276 aggradation older than the most recent fan-forming episode. These slip rate results are
277 discussed further in Section 6.

4.3. Tanzhuangzicun section

278 4.3.1. Overview and offset measurement

279 Our second slip rate site on the Luoshan Fault is at its northern end, beyond the end
280 of the Daluoshan and around 1.75 km west of the village of Tanzhuangzicun (see Figure 4
281 (a)). This section of the fault strikes at 355° and cuts across an alluvial apron into which
282 a number of channels have been incised (see Figure 8 (a)). The alluvial surface itself
283 has been modified and terraced for agriculture (see Figures 8 (b) and (c)) and some very
284 young streams have developed on top of this modified surface. However, evidence for
285 right-lateral fault motion has been preserved by the channel margins of the more heavily
286 incised streams. The whole fan surface slopes gently to the north and so the channels are
287 offset in the opposite direction to the regional gradient. We also see evidence of eroded

288 corners of channel risers on the down-slope edges of the channels (see Figures 8 (d) and
289 (e)) [e.g. *Cowgill* [2007]].

290 The mean offset recorded by ten different geomorphological markers (eight channel riser
291 tops, one channel riser bottom and one channel thalweg) on this single alluvial surface
292 was 50.6 ± 6.7 m and range of 37.2 to 61.4 m (see Table 1). Figures 8 (d) and (e) show
293 how a 51 m restoration aligns all of these markers, including those immediately adjacent
294 to the site of IRSL sample 3.

295 4.3.2. Age constraints and slip rate

296 IRSL sample 3 was taken at 37.425°N , 106.280°E , just to the east of the fault trace.
297 The sample was from fairly homogeneous, fine, yellow-brown loess, 169 cm below the
298 ground surface and approximately 15 cm below a thin gravel layer with 5 cm clasts of
299 angular material (see Figure 8 (g)). The sample returned an age of 10.6 ± 0.9 ka (see
300 Table 2). The mean offset (51 m) and the age of IRSL sample 3 allow us to calculate a
301 minimum slip rate along the Tanzhuangzicun section of 4.8 ± 0.8 mm/a (see Table 3).

4.4. Shiyadong site

302 4.4.1. Overview and offset measurement

303 *Min et al.* [2003] used TL dates from two sites (Shiyadong and Machanggou) at the
304 southern end of the Daluoshan section to obtain their slip rate estimate (see Figure 5
305 (b)). Here we use the high-resolution Pleiades DEM and our geomorphological mapping
306 to re-estimate the offsets at their sites.

307 At the southern end of the Daluoshan section, four different generations of alluvial fans
308 can be identified on the basis of their surface texture and degree of incision (see Figures 9

309 (a) and 9 (b), which are of the same area as Figure 5 (b)). The Shiyadong site is on
310 the F3 surface and *Min et al.* [2003] measured an offset of 18 ± 1 m. However, although
311 an 18 m restoration at this site re-aligns nearby gullies on a younger terrace surface, it
312 does not appear to re-align the gully that *Min et al.* [2003] sampled (see Figure 9 (d)).
313 The restoration is also complicated by the fact that the channels on the F3 surface are
314 highly sinuous, leading to a large degree of ambiguity in the amount of slip. However, we
315 re-measured the horizontal offsets of five piercing lines for channel thalwegs incised into
316 the F3 surface and obtained a mean offset of 41.1 ± 5.9 m and range of 33.8 to 48.5 m (see
317 Table 1 and Figures 9 (e) and 9 (f)).

318 4.4.2. Age constraints and slip rate

319 At Shiyadong (37.252°N , 106.320°E) *Min et al.* [2003] obtained a TL age of
320 9.80 ± 0.75 ka for the F3 surface. Using our new offset measurement we therefore esti-
321 mate a new slip rate of 4.2 ± 0.7 mm/a (see Table 3).

4.5. Machanggou site

322 4.5.1. Overview and offset measurement

323 At the Machanggou site, 1.7 km north of Shiyadong (see Figure 5 (b)), *Min et al.* [2003]
324 measured an offset of 171 ± 10 m. However, according to our geomorphological mapping
325 (see Figures 5 (b), 9 (a) and 9 (b)), the channel *Min et al.* [2003] investigated runs along
326 the side of the F4 surface rather than being incised into it. Their measured offset may
327 therefore not be representative of the displacement recorded by F4.

328 4.5.2. Age constraints and slip rate

329 At Machanggou (37.267°N, 106.321°E), *Min et al.* [2003] obtained a TL age of
330 69.0 ± 5.4 ka. However, their sample was from 3 m below the surface of F4 and so may
331 well be significantly older than that last episode of deposition on this surface (as we in-
332 terpreted for our IRSL sample 1). Due to the uncertainty in the offset measurement and
333 age constraint at this site, we are not able to estimate a slip rate at Machanggou.

5. The East Helanshan Fault

5.1. Background

334 The Yinchuan Graben is sited at the northern end of Ningxia Province, where the
335 deformation appears to be markedly different from that described for the Luoshan Fault.
336 Four major northeast-southwest trending normal faults cut Cenozoic and Quaternary
337 strata, accommodating apparently northwest-southeast extension. From west to east these
338 faults are: the East Helanshan Fault, the Luhatai Fault, the Yinchuan-Pingluo Fault,
339 and the Yellow River Fault (see Figure 3).

340 The East Helanshan Fault is approximately 120 km long and runs along the eastern side
341 of the Helanshan (Helan mountains). *Zhang et al.* [1990] estimate a Quaternary throw
342 rate for the East Helanshan Fault of 0.5 to 0.8 mm/a on the basis of the thickness of
343 Quaternary sediments in the basin. The throw rate on the Yellow River Fault is estimated
344 from TL ages of offset river terraces to be around 0.23 to 0.25 mm/a [*Liao et al.*, 2000].
345 Throw rates on the Yinchuan-Pingluo and Luhatai are estimated from composite drilling
346 profiles to be 0.14 mm/a (^{14}C date) and 0.18 mm/a (luminescence date) respectively [*Lei*
347 *et al.*, 2008, 2011, 2015]. According to a cross-sectional area balance, the whole Yinchuan
348 Graben is thought to have extended at 2.9 ± 1.0 mm/a since the Pliocene, though this

349 result relies on the interpretation of seismic reflection profiles [*Zhang et al.*, 1998]. The
350 graben contains 1 to 1.6 km of Quaternary sediments and approximately 6 km of pre-
351 Quaternary deposits that have accumulated since the Late Eocene [*Zhang et al.*, 1990].

352 A series of fresh scarps are present along the East Helanshan Fault [*Liao and Pan*,
353 1982]. The southernmost section of these scarps is called the Suyukou scarps, which vary
354 in strike between 10 and 50° and cut through four, large, coalesced, alluvial fans some
355 3 km from the range-front. From south to north, these fans are called the Baisikou,
356 Suyukou, Helankou and Chaqikou Fans [*Deng and Liao*, 1996] (see Figure 10 (b)). *Deng*
357 *and Liao* [1996] also identified four separate terrace levels in the scarp footwalls, from T1
358 (the youngest, typically 3 m high and thought to be from the 1739 Yinchuan earthquake)
359 to T4 (the oldest, up to 11 m high). The Baisikou, Suyukou and Helankou Fans are mainly
360 mantled by the T2 surface, with only scattered remnants of T3 and T4—although the
361 T1 surface is found adjacent to currently active channels. The Chaqikou Fan comprises
362 primarily the T1 and T2 surfaces. Landforms older than T4 are only preserved in a few
363 small areas. Firstly, at the range-front, some older terraces are preserved adjacent to
364 minor catchments. Secondly, north of the Chaqikou Fan, there is a remnant of a heavily
365 incised terrace (coloured dark brown in Figure 10 (b)), which is cut by multiple fault
366 scarps and pre-dates T4. We call this terrace T5.

367 On the basis of palaeoseismic trenching and radiocarbon dating at the Suyukou scarps
368 (and further north on the East Helanshan Fault), *Deng and Liao* [1996] concluded that
369 at least three earthquakes occurred on this fault prior to 1739: 2600 years ago, 4600-6300
370 years ago, and 8400 years ago. If these trench ages correlate with the terrace surfaces

371 preserved in the alluvial fans, then the offsets measured on the terraces can be used to
372 calculate a throw rate. *Deng and Liao* [1996] measure a combined terrace offset for the
373 last three events of 8.4 m. Combined with an age for the antepenultimate event of 6300
374 years, this yields a throw rate of 1.3 mm/a. In this study, however, we seek to provide the
375 first direct measurement of the Late Quaternary throw rate on the East Helanshan Fault
376 by conducting ^{10}Be dating of the terrace surfaces themselves and by making new vertical
377 offset measurements from high-resolution topography.

5.2. T5 at the northern end of the Suyukou scarps

378 5.2.1. Overview and offset measurement

379 Our first throw-rate site is on T5, at the northern end of the Suyukou scarps (see
380 Figure 11 and Figure 10 for location). Multiple fault scarps cut T5, all of which must
381 have formed since the abandonment of this surface. Topographic profiles from the Pleiades
382 DEM show a combined offset across all of these scarps of 19.4 ± 1.1 m (see Figure 11 and
383 the Supporting Information for methodology).

384 5.2.2. Age constraints and throw rate

385 A suite of eight quartz pebbles (samples 11A to 11H, from 38.783°N , 106.140°E) and
386 an amalgamated sample of 53 smaller clasts (sample 10, from 38.784°N , 106.134°E) were
387 taken for ^{10}Be dating from the surface of T5 (see Figure 11) and the results are shown
388 in Figure 12 (a) and Table 4. Five of the eight clasts are in relatively close agreement
389 with the aggregate age of 221.5 ± 3.9 ka. We therefore interpret the three younger clasts
390 (samples 11A, 11D and 11E) as outliers. An amalgamated sample of 42 pebbles (sample
391 12) and two individual clasts (samples 13A and 13B) were taken from the modern river

392 (at 38.777°N, 106.129°E, see Figure 11 for location) to estimate the inheritance in this
393 particular system. We obtained ^{10}Be ages of 27.5 ± 0.7 ka for the amalgamated sample, and
394 64.3 ± 1.2 ka and 8.0 ± 0.4 ka respectively for the two clasts. Although the small number of
395 samples indicate a large range in the inherited component, the inheritance is nonetheless
396 much less than the ages from the T5 surface itself. A zero inheritance model gives a T5
397 age of 221.5 ± 3.9 ka, whilst the largest measured inheritance (sample 13A) gives a T5
398 age of 157.2 ± 4.1 ka. These ages correspond to vertical throw rates of 0.09 ± 0.01 mm/a
399 and 0.12 ± 0.01 mm/a respectively (see Table 3). The large uncertainty in the inheritance
400 therefore has little effect on the calculated throw rate.

5.3. Central Suyukou scarps

401 5.3.1. Overview and offset measurement

402 Our second sampling site is at a location where a major river from the Helanshan crosses
403 the Suyukou scarps (see Figures 10, 13 (a) and 13 (b)). Here, the staircase pattern of
404 aggradational footwall terraces proposed by *Deng and Liao* [1996] (see Figure 13 (e)) can
405 be seen to the southwest of the current channel. These terraces are also partially evident
406 in the surface roughness map (see Figure 13 (c)). Topographic profiles extracted from the
407 Pleiades DEM confirm the stepped pattern, with heights for T1, T2 and T3 of 3.5 ± 0.8 m,
408 5.2 ± 0.5 m and 11.2 ± 1.5 m respectively (see Figure 13 (d) and the Supporting Information
409 for the full methodology).

410 5.3.2. Age constraints

411 ^{10}Be samples 14, 15 and 16 (consisting of amalgamations of 47, 49 and 73 quartz pebbles
412 respectively) were taken from T2, T3 and the modern river (see Figure 13 (b) and Table 4

413 for locations). They yielded ages of 18.5 ± 0.5 ka for T2, 42.3 ± 1.0 ka for T3 and 14.4 ± 0.7 ka
414 for the modern river. Correcting for inheritance gives a T2 age of 4.1 ± 0.9 ka and a T3 age
415 of 27.9 ± 1.2 ka. However, individual clasts taken from T2 (samples 14A to 14C) varied
416 in age between 8.7 ± 0.3 and 78.0 ± 1.5 ka (see Figure 12 (d)). Similarly, individual clasts
417 from the modern river (samples 16A to 16D) had ages between 9.6 ± 0.3 and 33.6 ± 0.8 ka
418 (see Figure 12 (e)).

419 These results suggest that there is significant variation in the magnitude of the inherited
420 component and that the ages obtained are not sufficiently reliable to determine the precise
421 timing of the earthquakes represented by T2 and T3. Nonetheless, the aggregate T3 age
422 of 42.3 ± 1.0 ka and the youngest clast from the modern river of 9.6 ± 0.3 (i.e. our lowest
423 measure of what the inheritance might be) give a T3 age of 32.7 ± 1.1 ka that we can
424 consider to be an upper bound. Combined with the vertical offset of 11.2 ± 1.5 m, this
425 suggests a minimum throw rate of 0.34 ± 0.05 mm/a over the last 30 ka (see Table 3).
426 The discrepancy between this and the 1.3 mm/a from the data of *Deng and Liao* [1996]
427 could be because there is not a one-to-one correlation between the colluvial wedges in the
428 trenches and the terraces preserved at the surface. Furthermore, our minimum throw rate
429 on the central Suyukou scarps is larger than the 0.09 to 0.12 mm/a obtained for T5 over
430 the last 200 ka (see Section 5.2), which is just along strike to the north. Assuming that
431 any earthquakes uplifting T3 also uplifted T5, this implies an increase in the throw rate
432 over time.

5.4. Helanshan range-front

433 5.4.1. Overview and offset measurement

434 Our third throw-rate site is at the Helanshan range-front, at the location indicated in
435 Figure 10. Here, a boulder fan straddles the range-front fault and a terrace is preserved
436 either side of the channel on the footwall side (see Figure 14). This terrace pre-dates T1-4.
437 Topographic profiles extracted from the Pleiades DEM indicate that the terrace records
438 an offset on the range-front fault of 24.0 ± 4.0 m (see Figure 14 (e) and the Supporting
439 Information for methodology).

440 5.4.2. Age constraints and throw rate

441 An amalgamated sample of 83 quartz pebbles (sample 9, from 38.736°N , 106.012°E)
442 and a single boulder top (sample 1, from 38.736°N , 106.011°E) were collected from the
443 terrace surface southwest of the channel (see Figure 14 (b) for locations). We were not
444 able to collect more boulder top samples because there were very few large boulders with
445 well-preserved desert varnish on top of the terrace. The samples yielded ^{10}Be ages of
446 120.6 ± 1.9 ka and 111.5 ± 2.0 ka respectively. Despite the small number of samples, the
447 relatively close agreement between the two gives us confidence that the aggregate age is
448 reliable.

449 We use the aggregate age of 120.6 ± 1.9 ka to calculate a vertical throw rate of
450 0.20 ± 0.03 mm/a (see Table 3), which is a minimum rate because it does not account for
451 inherited ^{10}Be . If we allowed for a much larger inheritance (of 64.3 ± 1.2 ka, as measured for
452 sample 13A in a different catchment) we obtain a vertical throw rate of 0.43 ± 0.07 mm/a
453 (see Table 3). In other words, even though the uncertainty on the inheritance is large,
454 the maximum throw rate is still small (less than 0.5 mm/a).

455 In addition, six boulder tops (samples 3 to 8) were collected from the boulder fan that
456 straddles the range-front fault (see Figure 14 (b) and Table 4 for locations). Since no scarps
457 are preserved in the boulder fan itself, it must post-date the most recent surface-rupturing
458 event at this location. The boulder tops range in age from 8.2 ± 1.1 ka to 38.3 ± 1.4 ka (see
459 Figure 12 (b)). A plot of ^{10}Be exposure age against distance down slope from the fault
460 trace shows that more distal samples have older exposure ages (see Figure 12 (c)). This
461 suggests that the boulder fan has been generated in more than one event, with the most
462 recent episode of deposition being restricted to near the apex of the fan. Samples 4, 5
463 and 6, all from near the apex of the fan, have ages of 13.1 ± 0.9 , 8.2 ± 1.1 and 11.1 ± 0.5 ka
464 respectively, and we propose that these three ages represent the probable abandonment
465 age of the boulder fan.

5.5. Northern end of the East Helanshan Fault

466 5.5.1. Overview and offset measurement

467 At the northern end of the East Helanshan Fault we found evidence for right-lateral
468 motion (see Figure 3 for location). Here, three boulder ridges on top of an alluvial fan
469 surface and an incised gully are right-laterally offset (see Figure 15). The scarp is fresh,
470 with a free face, and this site is at the northernmost end of the rupture trace from the 1739
471 Yinchuan earthquake [*Middleton et al.*, 2015]. The incised channel is offset by 4 m (see
472 Figures 15 (b) and 15 (c)), probably representing displacement in the 1739 event. The
473 boulder ridges form indistinct linear markers, but the shadows at the sides of the boulder
474 ridges are not completely aligned by a restoration of 4 m; our best visual restoration is at
475 16 m, though with visually estimated uncertainties of at least ± 5 m (see Figure 15 (d)).

476 **5.5.2. Age constraints and slip rate**

477 IRSL samples 4 and 5 were taken from an exposure in the wall of an incised river channel
478 that cuts across the displaced fan (39.236°N, 106.658°E) at depths of 54 cm and 127 cm
479 respectively. IRSL sample 4 was from a 10 cm thick lens of medium brown silt, covered
480 by a 50 cm thick layer of large, poorly sorted cobbles (see Figure 15 (e)); IRSL sample 5
481 was from a stratigraphically lower, 20 cm thick layer of orange sand surrounded by coarse
482 gravels and cobbles (see Figure 15 (f)). Sample 4 returned an age of 1.27 ± 0.14 ka and
483 sample 5 returned an age of 3.21 ± 0.21 ka (see Table 2). These results are stratigraphically
484 consistent.

485 The 1.27 ka age implies a horizontal slip rate of 12.6 ± 4.2 mm/a (see Table 3), which
486 appears unrealistically large. However, we note that both samples are taken from the
487 fill of a channel between the boulder ridges, which might post-date abandonment of the
488 fan itself. It is hence likely that both IRSL ages underestimate the deposition age of the
489 underlying displaced boulder ridge.

6. Discussion

6.1. Rates of faulting along the western Ordos Plateau

490 Our key result from the Luoshan Fault is that the slip rate is comparatively large (i.e >
491 4 mm/a), which shows that this fault is one of the principal active structures in the west-
492 ern Ordos region. The agreement between our slip rate results from IRSL samples 2 and
493 3 (to within their 1σ analytical errors) and our re-assessment of the Shiyadong site indi-
494 cate that the mean right-lateral Holocene slip rate on the Luoshan Fault is 4.3 ± 0.4 mm/a
495 (where the error now refers to the weighted standard deviation of the three slip rate esti-

496 mates, see Table 3). Furthermore, at all three sites the fans were dated to approximately
497 10 ka ago (and the measured horizontal offsets are similar). This common age suggests
498 that the deposition of these fans is principally controlled by climate.

499 On the East Helanshan Fault our major result is that the throw rate, and hence the
500 extension rate, is comparatively small (i.e. < 1 mm/a). Since the Suyukou scarps run
501 parallel to the Helanshan range-front, we add our maximum throw rate estimate from
502 Suyukou (of 0.34 ± 0.05 mm/a) to our maximum throw rate estimate from the range-front
503 (of 0.43 ± 0.07 mm/a) to obtain a Late Quaternary throw rate for the fault as a whole of
504 0.8 ± 0.1 mm/a (see Table 3). This is consistent with the Quaternary average of 0.5 to
505 0.8 mm/a from *Zhang et al.* [1990]. Using the shallowest fault dip found in the literature
506 of 39° (and hence giving the maximum possible extension rate for this throw rate), we
507 find an extension rate across the East Helanshan Fault of 0.9 ± 0.1 mm/a (see Table 3). If
508 we also include the throw rates and fault dips of the other faults within the graben (Yellow
509 River Fault: 0.25 mm/a and 72° [*Liao et al.*, 2000; *Fang et al.*, 2009]; Yinchuan-Pingluo
510 Fault: 0.14 mm/a and 71° [*Lei et al.*, 2008, 2015]; Luhuatai Fault: 0.18 mm/a and 60°
511 [*Fang et al.*, 2009; *Lei et al.*, 2011]) we obtain an extension rate across the whole graben of
512 1.2 ± 0.1 mm/a. Additionally, our suggested increase in throw rate on the Suyukou scarps
513 (see Section 5.3) could indicate that motion is being transferred from the range-front fault
514 to the Suyukou scarps in the alluvial fans—possibly in order to cut off a corner in the
515 range-front and straighten the fault.

516 Campaign GPS measurements [*Zhao et al.*, 2015] also indicate that right-lateral shearing
517 is the major motion occurring in the western Ordos region (see Figure 16). Figure 16 (a)

518 shows the data from *Zhao et al.* [2015] with a best fitting rigid body rotation (about an
519 Euler pole at 46°N, 72°W, estimated from the vectors within this region) subtracted from
520 all of the vectors. This ensures that rotations associated with this rigid-body-like motion
521 do not distort our slip rate estimates. We model the fault parallel interseismic motion
522 across the Luoshan Fault as a buried screw dislocation in an elastic half-space using the
523 formulation from *Savage and Burford* [1973], where the velocity u at a perpendicular
524 distance x from the fault is given by $u = \frac{s}{\pi} \tan^{-1} \left(\frac{x}{d} \right)$, where s is the slip rate and d
525 is the locking depth. The density of data is not sufficient to provide an independent
526 constraint on the locking depth, so we assume locking depths in the range of 10 to 20 km
527 [*Wright et al.*, 2013] in order to calculate the distribution of possible slip rate estimates.
528 In Figure 16 (b), the range of possible arctangent functions fitted to the data indicates a
529 right-lateral slip rate on the Luoshan and northern Yunwushan Faults of 4.0 ± 0.5 mm/a.
530 Our geological slip rate of 4.3 ± 0.4 mm/a agrees well with this geodetic rate. We also
531 note that one GPS point lies noticeably to the west of our best fitting curves. This
532 may indicate that the centre of the shear zone at depth is displaced to the west of the
533 surface trace of the Luoshan Fault, but there is not enough data to reliably test this.
534 Figure 16 (c) shows that, although the errors on the data are large, there is no resolvable
535 fault-perpendicular motion along profile X-X'; significant crustal shortening only occurs
536 further to the south of our profile. The data in Figure 16 (d), for profile Y-Y' across
537 the Yinchuan Graben, are more scattered than in Figure 16 (b). If we assume that all
538 of the right-lateral motion is localised onto a single structure, we obtain a right-lateral
539 slip-rate of 3.0 ± 0.4 mm/a (allowing for the same 10 to 20 km range of locking depths).

540 However the scatter in the data suggests that it is more likely that right-lateral motion is
541 distributed across a number of the buried faults within the Yinchuan Graben. In Figure 16
542 (e), the scatter in the data is again very large—and extension is barely resolvable—but we
543 obtain a best fitting extension rate of 1.3 ± 1.6 mm/a across the Yinchuan Graben. This
544 is consistent with our Late Quaternary extension rate of 1.2 ± 0.1 mm/a and also supports
545 our suggestion that right-lateral motion is dominant over the extension in the Yinchuan
546 Graben.

6.2. A geometric model for the western Ordos Plateau

547 We propose a geometric model in which the faults of the western Ordos Plateau ac-
548 commodate principally north-south right-lateral shearing. This occurs on the Luoshan
549 Fault in the south and is split between the Alxa Desert and East Helanshan Faults in the
550 north (see Figure 17). Satellite imagery shows evidence of right-lateral displacements on
551 the Alxa Desert Fault, but its slip rate is unknown (see Figure 17 (c)). Meanwhile, our
552 observations of offset boulder ridges at the northern end of the East Helanshan Fault (see
553 Section 5.5) provide evidence for the continuation of right-lateral motion up the western
554 side of the Ordos Plateau north of the Yinchuan Graben. A Kostrov summation for the
555 two largest earthquakes in northern Ningxia in the last 700 years indicates that north-
556 south right-lateral motion is one of the most significant strains [*Wesnowsky et al.*, 1984].
557 Furthermore, one of the few focal mechanisms from the instrumental record (for a M 5.2
558 event in 1988—see Figure 3) is also consistent with north-south right-lateral motion.

559 In addition, we suggest that the (oblique reverse) Niushoushan Fault accommodates
560 transpression as the strike-slip faulting steps to the left and that the normal faulting in

561 the Yinchuan Graben accommodates transtension as the strike-slip faulting steps to the
562 right. The estimated slip vector for the most recent earthquake on the East Helanshan
563 Fault appears to show pure normal motion [*Middleton et al.*, 2015]. We therefore speculate
564 that the transtension in the Yinchuan Graben is partitioned between normal motion on
565 the East Helanshan Fault and right-lateral strike-slip motion on one or more of the buried
566 faults within the graben (i.e. the Luhuatai, Yinchuan-Pingluo or Yellow River Fault).

7. Implications for the kinematics of the Ordos block

567 In Section 1 we saw that the Ordos Plateau is situated within a large-scale zone of
568 WNW-ESE left-lateral shearing. To the south and west of the plateau, this shearing is
569 manifested as slip on the Haiyuan Fault at 5-10 mm/a [*Zhang et al.*, 1988, 1990; *Burchfiel*
570 *et al.*, 1991; *Min et al.*, 2000; *Cavalié et al.*, 2008; *Li et al.*, 2009] (see also Figure 1
571 (b)), the West Qinling Fault at 2-3 mm/a [*Deng et al.*, 2004; *Harkins et al.*, 2010], and
572 the Qinlingshan Fault at 5-9 mm/a [*Zhang et al.*, 1995; *Deng et al.*, 2004]; to the north
573 there is geological and geodetic evidence for around 2 mm/a of left-lateral motion on the
574 Zhangjiakou-Bohai Fault system [*Zheng et al.*, 1981; *Xu et al.*, 1993; *Shen et al.*, 2000] (see
575 Figure 19). Several kinematic models have proposed that the Ordos Plateau is rotating
576 anticlockwise within this zone of shearing [*Xu and Ma*, 1992; *Xu et al.*, 1993; *Avouac and*
577 *Tapponnier*, 1993; *Xu et al.*, 1994; *Zhang et al.*, 1995; *Peltzer and Saucier*, 1996; *Zhang*
578 *et al.*, 1998].

579 We have shown that the anticlockwise rotation of the Ordos block can be confirmed by
580 considering the fault kinematics at the boundary of the block. For an equidimensional
581 crustal block that is rotating within a large-scale shear zone, the second order strike-

582 slip motion on either side of the block is expected to be of a similar magnitude and
583 opposite sense to the overall shear gradient across the block (see Supporting Information
584 for mathematical details). In the case of the Ordos Plateau, the GPS data in Figure 18 (a)
585 indicate an overall left-lateral shear gradient across the block of ≈ 5 mm/a. Meanwhile,
586 we have shown in this study that the dominant motion on the western side of the block
587 is right-lateral, at a rate of ≈ 4 mm/a. Right-lateral shearing also occurs on the eastern
588 side of the block by normal slip on the en-echelon Shanxi Grabens and right-lateral slip
589 on the Xizhoushan Fault (at 5.7 mm/a) and the Huoshan Fault (at 7 mm/a) [Xu *et al.*,
590 1986; Xu and Deng, 1990]. In other words, the Ordos Plateau behaves as expected, with
591 the second order strike-slip motion on either side of the block occurring at a similar rate
592 but in the opposite sense to the motion of the overall shear zone.

593 Figure 19 illustrates our kinematic model. The dotted lines in Figure 19 (a) indicate
594 the possible existence of the Taihangshan and North China Plain blocks to the east of
595 the Ordos Plateau. Little is known about the faulting to the west of the Ordos Plateau,
596 but a series of mapped left-lateral faults in the Alxa Desert could be accommodating
597 distributed shearing. Figures 19 (b), 19 (c) and 19 (d) show schematic representations
598 of the kinematics, in which three blocks are rotating anticlockwise within a WNW-ESE
599 left-lateral shear zone. For the rotations to be accommodated, either compression must
600 occur at the NE and SW corners of each block, or the overall zone has to widen. For left-
601 lateral shear at 5 mm/a, a kinematic model with equidimensional crustal blocks predicts
602 widening of the zone at a rate of 1.8 mm/a (see Supporting Information for mathematical
603 details).

604 The 1998 M_w 5.7 Zhangbei earthquake had a reverse-faulting mechanism and occurred
605 near the northeastern corner of the Ordos Plateau [*Li et al.*, 2008]—see Figure 19 (a).
606 This event could therefore represent part of the compression necessary for anticlockwise
607 rotation of the Ordos Plateau. However, the GPS data in Figure 18 (b) indicate NNE-
608 SSW extension across the whole zone of 1.9 ± 0.8 mm/a. This is in close agreement with
609 the prediction of the kinematic model and therefore suggests that widening of the zone is
610 the dominant mechanism allowing rotation.

611 Figures 19 (e) and 19 (f) show how the geometry of the system can be modified to
612 account for the fact that the slip rate on the Haiyuan Fault is notably larger than that on
613 the West Qinling Fault, thereby providing a possible explanation for the development of
614 the Liupanshan. Figures 19 (g) and (h) show how initially corrugated block boundaries
615 (as perhaps determined by the location of pre-existing structures) can lead to the develop-
616 ment of en-echelon grabens and intervening right-lateral faults on the eastern and western
617 margins of the block. (Faults in both the Yinchuan Graben and the Shanxi Grabens are
618 known to have reactivated pre-existing structures [*Xu and Ma*, 1992; *Xu et al.*, 1993; *Liu*,
619 2000; *Darby and Ritts*, 2002].) Figures 19 (i) and (j) combine the above modifications
620 into a single schematic representation of the kinematics.

621 Similar tectonic arrangements of rotating crustal blocks are also seen elsewhere—for
622 example in northern Israel [*Ron et al.*, 1984], eastern Iran [*McKenzie and Jackson*, 1983;
623 *Walker and Jackson*, 2004], the Walker Lane of western North America [*Wesnousky*,
624 2005; *Wesnousky et al.*, 2012], and the southeastern Tibetan Plateau [*Copley*, 2008].
625 The apparent predominance of normal faulting around the margins of the Ordos Plateau

626 disguises the fact that it is the strike-slip motions that are most important. The normal
627 faulting is present either as part of a partitioned transtensional system (as may be the
628 case for the East Helanshan Fault) or because it is arranged en echelon to accommodate
629 an overall shear (as is the case in the Shanxi Grabens—see also *Goldsworthy et al.* [2002];
630 *Wesnowsky* [2005]). This is a similar situation to that suggested for the northern Walker
631 Lane [*Wesnowsky et al.*, 2012], though the shearing is in the opposite sense.

8. Conclusions

632 In the absence of reliable palaeomagnetic constraints, we have used the fault kinematics
633 in the western Ordos region to examine the hypothesis that the Ordos block acts as a rigid
634 crustal block within a large-scale left-lateral shear zone, rotating anticlockwise about a
635 vertical axis. Our key result is that the rate of strike-slip motion on the Luoshan Fault
636 (4.3 ± 0.4 mm/a) is substantially larger than the throw rate on the normal East Helanshan
637 Fault (0.8 ± 0.1 mm/a). We therefore conclude that north-south right-lateral shearing
638 is the principal tectonic motion in the western Ordos region, which is compatible with
639 anticlockwise rotation of the whole Ordos block.

Acknowledgments.

640 This research has been supported by the Natural Environment Research Council
641 (NERC) through a studentship awarded to TAM, the Centre for Observation and Mod-
642 elling of Earthquakes, Volcanoes and Tectonics (COMET, GA/13/M/031), the Looking
643 inside the Continents from Space (LiCS) large grant (NE/K011006/1), the NERC/ESRC
644 Earthquakes without Frontiers (EwF) consortium (EwF_NE/J02001X/1.1), the National
645

646 Natural Science Foundation of China (41472201), and the State Key Laboratory of Earth-
 647 quake Dynamics (LED2014A03).

648 We are grateful to: Peizhen Zhang and colleagues at the China Earthquake Adminis-
 649 tration (CEA) for assistance with fieldwork; Victoria Forbes, Maria Miguens-Rodriguez,
 650 Kathy Keefe and Owen Green for their help preparing the ^{10}Be samples for dating; Rob
 651 Ashurst for his assistance with the IRSL dating; and Al Sloan, Austin Elliott and David
 652 Mackenzie for helpful discussions.

653 The Pleiades topography can be downloaded from OpenTopography (<http://www.opentopography.org/>).
 654 Most of the figures in this paper were made using GMT [*Wessel et al.*, 2013].

References

References

- 655 Avouac, J.-P., and P. Tapponnier (1993), Kinematic model of active deformation in central Asia, *Geophysical Research*
 656 *Letters*, *20*(10), 895, doi:10.1029/93GL00128.
- 657 Bai, M., and D. Jiao (2005), The historical analysis for M=8 earthquake in 1739 at Yinchuan-Pingluo area, *Northwestern*
 658 *Seismological Journal*, *27*(2), 135–140 (in Chinese).
- 659 Balco, G., J. O. Stone, N. a. Lifton, and T. J. Dunai (2008), A complete and easily accessible means of calculating surface ex-
 660 posure ages or erosion rates from ^{10}Be and ^{26}Al measurements, *Quaternary Geochronology*, *3*(3), 174–195, doi:
 661 10.1016/j.quageo.2007.12.001.
- 662 Burchfiel, B. C., P. Zhang, Y. Wang, W. Zhang, F. Song, Q. Deng, P. Molnar, L. Royden, and L. Royden (1991), Geology of the Haiyuan
 663 Fault zone, Ningxia-hui autonomous region, China, and its relation to the evolution of the northeastern margin of the Tibetan Plateau,
 664 *Tectonics*, *10*(6), 1091–1110.
- 665 Cavalié, O., C. Lasserre, M.-P. Doin, G. Peltzer, J. Sun, X. Xu, and Z.-K. Shen (2008), Measurement of interseismic strain across
 666 the Haiyuan fault (Gansu, China), by InSAR, *Earth and Planetary Science Letters*, *275*, 246–257, doi:
 667 10.1016/j.epsl.2008.07.057.
- 668 Chai, C., G. Meng, P. Du, Y. Wang, B. Liu, W. Shen, Q. Lei, Y. Liao, C. Zhao, S. Feng, X. Zhang, and X. Xie (2006), Comprehensive
 669 multi-level exploration of buried active fault: an example of Yinchuan buried active fault, *Seismology and Geology*,
 670 *28*(4), 536–546 (in Chinese).
- 671 Chen, H., J. Hu, W. Gong, R. Kang, and L. Li (2015), Characteristics and transition mechanism of late Cenozoic structural deformation
 672 within the NiushoushanLuoshan fault zone at the northeastern margin of the Tibetan Plateau, *Journal of Asian Earth*
 673 *Sciences*, doi:10.1016/j.jseaes.2015.06.034.
- 674 Copley, A. (2008), Kinematics and dynamics of the southeastern margin of the Tibetan Plateau, *Geophysical Journal In-*
 675 *ternational*, *174*, 1081–1100, doi:10.1111/j.1365-246X.2008.03853.x.
- 676 Cowgill, E. (2007), Impact of riser reconstructions on estimation of secular variation in rates of strike slip faulting: Revisiting the
 677 Cherchen River site along the Altyn Tagh Fault, NW China, *Earth and Planetary Science Letters*, *254*, 239–
 678 255, doi:10.1016/j.epsl.2006.09.015.
- 679 Darby, B., B. Ritts, Y. Yue, and Q. Meng (2005), Did the Altyn Tagh fault extend beyond the Tibetan Plateau?, *Earth and*
 680 *Planetary Science Letters*, *240*(2), 425–435, doi:10.1016/j.epsl.2005.09.011.
- 681 Darby, B. J., and B. D. Ritts (2002), Mesozoic contractional deformation in the middle of the Asian tectonic collage: the intraplate
 682 Western Ordos foldthrust belt, China, *Earth and Planetary Science Letters*, *205*(1-2), 13–24, doi:10.1016/S0012-
 683 821X(02)01026-9.
- 684 DeMets, C., R. G. Gordon, D. F. Argus, and S. Stein (1990), Current plate motions, *Geophysical Journal International*,
 685 *101*(2), 425–478, doi:10.1111/j.1365-246X.1990.tb06579.x.

- 686 DeMets, C., R. G. Gordon, D. F. Argus, and S. Stein (1994), Effect of recent revisions to the geomagnetic reversal time scale on estimates
687 of current plate motions, *Geophysical Research Letters*, *21* (20), 2191–2194.
- 688 Deng, Q., and Y. Liao (1996), Paleoseismology along the range-front fault of Helan Mountains, north central China, *Journal of*
689 *Geophysical Research*, *101*, 5873–5893.
- 690 Deng, Q., F. Sung, S. Zhu, M. Li, T. Wang, W. Zhang, B. C. Burchfiel, P. Molnar, and P. Zhang (1984), Active faulting and tectonics
691 of the Ningxia-Hui autonomous region, China, *Journal of Geophysical Research*, *89*, 4427–4445.
- 692 Deng, Q., Y. Ran, X. Yang, W. Min, and Q. Chu (2004), Map of Active Tectonics in China (in Chinese).
- 693 Ekström, G., M. Nettles, and A. Dziewonski (2012), The global CMT project 2004–2010: Centroid-moment tensors for 13,017 earthquakes,
694 *Physics of the Earth and Planetary Interiors*, *200–201*, 1–9, doi:10.1016/j.pepi.2012.04.002.
- 695 England, P., and P. Molnar (1997), The field of crustal velocity in Asia calculated from Quaternary rates of slip on faults, *Geophys-*
696 *ical Journal International*, *130*, 551–582.
- 697 Fan, J., and J. Ma (2003), Movement of Ordos block and alternation of activity along its boundaries, *Science in China*
698 *(Series D)*, *46* (October), 168–180, doi:10.1360/03dz0013.
- 699 Fang, S., C. Zhao, C. Chai, B. Liu, S. Feng, M. Liu, Q. Lei, and H. Liu (2009), Seismological Evidences of the Crustal Struc-
700 tures and Tectonics in the Yinchuan Downfaulted Basin, *Chinese Journal of Geophysics*, *52*(5), 1101–1110,
701 doi:10.1002/cjg2.1435.
- 702 Farr, T. G., P. A. Rosen, E. Caro, R. Crippen, R. Duren, S. Hensley, M. Kobrick, M. Paller, E. Rodriguez, L. Roth, D. Seal, S. Shaf-
703 fer, J. Shimada, J. Umland, M. Werner, M. Oskin, D. Burbank, and D. Alsdorf (2007), The Shuttle Radar Topography Mission,
704 *Reviews of Geophysics*, *45*, 1–33, doi:10.1029/2005RG000183.1.INTRODUCTION.
- 705 Frankel, K. L., and J. F. Dolan (2007), Characterizing arid region alluvial fan surface roughness with airborne laser swath map-
706 ping digital topographic data, *Journal of Geophysical Research: Earth Surface*, *112*(2), 1–14, doi:
707 10.1029/2006JF000644.
- 708 Gan, W., P. Zhang, Z.-K. Shen, Z. Niu, M. Wang, Y. Wan, D. Zhou, and J. Cheng (2007), Present-day crustal motion within
709 the Tibetan Plateau inferred from GPS measurements, *Journal of Geophysical Research*, *112*(B8), 1–14, doi:
710 10.1029/2005JB004120.
- 711 Goldsworthy, M., J. Jackson, and J. Haines (2002), The continuity of active fault systems in Greece, *Geophysical Journal*
712 *International*, *148*(3), 596–618, doi:10.1046/j.1365-246X.2002.01609.x.
- 713 Harkins, N., E. Kirby, X. Shi, E. Wang, D. Burbank, and F. Chun (2010), Millennial slip rates along the eastern Kunlun fault: Implications
714 for the dynamics of intracontinental deformation in Asia, *Lithosphere*, *2*(4), 247–266, doi:10.1130/L85.1.
- 715 International Seismological Centre (2013), On-Line Bulletin.
- 716 Jackson, J., and D. McKenzie (1988), The relationship between plate motions and seismic moment tensors, and the rates of active deformation
717 in the Mediterranean and Middle East, *Geophysical Journal International*, *93*(1), 45–73, doi:10.1111/j.1365-
718 246X.1988.tb01387.x.
- 719 Lal, D. (1991), Cosmic ray labeling of erosion surfaces: in situ nuclide production rates and erosion models, *Earth and Plane-*
720 *tary Science Letters*, *104*, 424–439.
- 721 Lasserre, C., Y. Gaudemer, P. Tapponnier, A.-S. Mériaux, J. Van der Woerd, Y. Daoyang, F. Ryerson, R. Finkel, and M. Caffee (2002),
722 Fast late Pleistocene slip rate on the Leng Long Ling segment of the Haiyuan fault, Qinghai, China, *Journal of Geophysical*
723 *Research*, *107*, doi:10.1029/2000JB000060.
- 724 Lei, Q., C. Chai, G. Meng, P. Du, Y. Wang, X. Xie, and X. Zhang (2008), Composite drilling section exploration of Yinchuan Buried
725 Fault, *Seismology and Geology*, *30*(1), 250–263 (in Chinese).
- 726 Lei, Q., C. Chai, P. Du, Y. Wang, and G. Meng (2011), Activity characteristics of Luhuatai Buried Fault since Late Quaternary revealed
727 by drilling, *Seismology and Geology*, *33*(3), 602–614 (in Chinese).
- 728 Lei, Q., C. Chai, P. Du, J. Yu, X. Xie, and Y. Wang (2015), Re-discussion of the seismogenic structure of the M8.0 Pingluo earthquake
729 in 1739, *Seismology and Geology*, *37*(2), (in Chinese).
- 730 Li, C., P. Zhang, J. Yin, and W. Min (2009), Late Quaternary left-lateral slip rate of the Haiyuan fault, northeastern margin of the
731 Tibetan Plateau, *Tectonics*, *28*, doi:10.1029/2008TC002302.
- 732 Li, W., Y. Lu, and G. Ding (2001), Paleomagnetic evidence from loess for the relative motion between the Ordos and its adjacent blocks,
733 *Quaternary Sciences*, *21*(6), 551–559 (in Chinese).
- 734 Li, W., Y. Dong, A. Guo, X. Liu, and D. Zhou (2013), Chronology and tectonic significance of Cenozoic faults in the Liupanshan Arcuate
735 Tectonic Belt at the northeastern margin of the Qinghai-Tibet Plateau, *Journal of Asian Earth Sciences*, *73*,
736 103–113, doi:10.1016/j.jseas.2013.04.026.
- 737 Li, Z., W. Feng, Z. Xu, P. Cross, and J. Zhang (2008), The 1998 Mw 5.7 Zhangbei-Shangyi (China) earthquake revisited: A buried
738 thrust fault revealed with interferometric synthetic aperture radar, *Geochemistry Geophysics Geosystems*, *9*(4),
739 1–11, doi:10.1029/2007GC001910.
- 740 Liao, Y., and Z. Pan (1982), Dislocation of the great wall in the Hongguozigou, Ningxia autonomous region, *Seismology and*
741 *Geology*, *4*(2), 77–80 (in Chinese).
- 742 Liao, Y., C. Chai, W. Zhang, and W. Xu (2000), The active features and slip rate of Lingwu faults in late Quaternary, *Earthquake*
743 *Research in China*, *16*(2), 158–165.
- 744 Lin, A., G. Rao, J. Hu, and W. Gong (2013), Reevaluation of the offset of the Great Wall associated with the ca. M 8.0 Pingluo
745 earthquake of 1739, Yinchuan graben, China, *Journal of Seismology*, *17*(4), 1281–1294, doi:10.1007/s10950-013-9391-2.
- 746 Lin, A., J. Hu, and W. Gong (2015), Active normal faulting and the seismogenic fault of the 1739 M 8.0 Pingluo earthquake
747 in the intracontinental Yinchuan Graben, China, *Journal of Asian Earth Sciences*, *114*, 155–173, doi:
748 10.1016/j.jseas.2015.04.036.

- 749 Liu, G. (2000), The Cenozoic rift system of the North China Plain and the deep internal process, *Tectonophysics*, *133*(1987),
750 277–285.
- 751 Liu, J., P. Zhang, D. Zheng, J. Wan, W. Wang, P. Du, and Q. Lei (2010), Pattern and timing of late Cenozoic rapid exhumation and
752 uplift of the Helan Mountain, China, *Science China Earth Sciences*, *53*(3), 345–355, doi:10.1007/s11430-010-0016-0.
- 753 Liu, M., S. Stein, and H. Wang (2011), 2000 years of migrating earthquakes in North China: How earthquakes in midcontinents differ
754 from those at plate boundaries, *Lithosphere*, *3*(2), 128–132, doi:10.1130/L129.1.
- 755 Liu-Zeng, J., Y. Klinger, X. Xu, C. Lasserre, G. Chen, W. Chen, P. Tapponnier, and B. Zhang (2007), Millennial recurrence of large
756 earthquakes on the Haiyuan fault near Songshan, Gansu Province, China, *Bulletin of the Seismological Society
757 of America*, *97*(1B), 14–34, doi:10.1785/0120050118.
- 758 McKenzie, D., and J. Jackson (1983), The relationship between strain rates, crustal thickening, palaeomagnetism, finite strain and fault
759 movements within a deforming zone, *Earth and Planetary Science Letters*, *65*(1), 182–202, doi:10.1016/0012-
760 821X(83)90198-X.
- 761 Middleton, T. A., R. T. Walker, B. Parsons, Q. Lei, Y. Zhou, and Z. Ren (2015), A major, intraplate, normal-faulting earthquake: the
762 1739 Yinchuan event in northern China, *Journal of Geophysical Research (Solid Earth)*, *121*(1), 293–320,
763 doi:10.1002/2015JB012355. Received.
- 764 Min, W., Z. Chai, P. Wang, P. Yang, C. Chai, P. Wang, and P. Yang (1992), Preliminary study on the Holocene active fault features at
765 the eastern piedmont of the Luoshan mountain, *Earthquake Research in China*, *8*(4), 49–54 (in Chinese).
- 766 Min, W., Z. Chai, P. Wang, and P. Yang (1993), The study on the paleoearthquakes on the eastern piedmont fault of the Luoshan
767 mountains in Holocene, *Earthquake Research in China*, *5*(4), 97–102 (in Chinese).
- 768 Min, W., P.-Z. Zhang, and Q.-D. Deng (2000), Primary study on regional paleoearthquake recurrence behavior, *Acta Seismo-
769 logica Sinica*, *13*(2), 180–188, doi:10.1007/s11589-000-0008-9.
- 770 Min, W., P. Zhang, and Q. Deng (2001), The study of Holocene paleoearthquakes on Zhongwei-Tongxin fault zone, *Seismology
771 and Geology*, *23*(3), 357–366 (in Chinese).
- 772 Min, W., D. Jiao, C. Chai, P. Zhang, and F. Mao (2003), Characteristics of the active Luoshan Fault since Late Pleistocene, North
773 Central China, *Annals of Geophysics*, *46*(5), 997–1013.
- 774 Molnar, P., and K. E. Dayem (2010), Major intracontinental strike-slip faults and contrasts in lithospheric strength, *Geosphere*,
775 *6*(4), 444–467, doi:10.1130/GES00519.1.
- 776 Molnar, P., and J. Stock (2009), Slowing of India's convergence with Eurasia since 20 Ma and its implications for Tibetan mantle
777 dynamics, *Tectonics*, *28*, doi:10.1029/2008TC002271.
- 778 Nie, Z., and W. Lin (1993), Middle segment of Zhongwei-Tongxin fault zone: seismic deformation band of 1709 earthquake with M 7.5
779 along Xiangshan-Tianjingshan fault zone, *Earthquake*, pp. 41–44 (in Chinese).
- 780 Peltzer, G., and F. Saucier (1996), Present-day kinematics of Asia derived from geologic fault rates, *Journal of Geophysical
781 Research*, *101*, 27,943–27,956, doi:10.1029/96JB02698.
- 782 Ren, Z., Z. Zhang, T. Chen, S. Yan, J. Yin, P. Zhang, W. Zheng, H. Zhang, and C. Li (2015), Clustering of offsets on the Haiyuan fault and
783 their relationship to paleoearthquakes, *Geological Society of America Bulletin*, (June), doi:10.1130/B31155.1.
- 784 Ron, H., R. Freund, Z. Garfunkel, and A. Nur (1984), Block rotation by strike-slip faulting: structural and paleomagnetic evidence,
785 *Journal of Geophysical Research*, *89*(B7), 6256–6270, doi:10.1029/JB089iB07p06256.
- 786 Savage, J. C., and R. O. Burford (1973), Geodetic determination of relative plate motion in central California, *Journal of Geo-
787 physical Research*, *78*(5), 832–845.
- 788 Shen, Z., C. Zhao, A. Yin, Y. Li, D. D. Jackson, P. Fang, and D. Dong (2000), Contemporary crustal deformation in east Asia constrained
789 by Global Positioning System measurements, *Journal of Geophysical Research*, *105*, 5721–5734.
- 790 Stone, J. O. (2000), Air pressure and cosmogenic isotope production, *Journal of Geophysical Research*, *105*(B10),
791 23,753–23,759.
- 792 Tapponnier, P., and P. Molnar (1977), Active faulting and tectonics in China, *Journal of Geophysical Research*,
793 *82*(20), 2905–2930.
- 794 Thatcher, W. (2009), How the Continents Deform : The Evidence From Tectonic Geodesy, *Annual Review of Earth and
795 Planetary Sciences*, *37*, 237–262, doi:10.1146/annurev.earth.031208.100035.
- 796 The Research Group on "Active Fault System around Ordos Massif" (1988), *Active Fault System around Ordos
797 Massif*, (in Chinese) pp., State Seismological Bureau, Seismological Press, Beijing.
- 798 Walker, R., and J. Jackson (2004), Active tectonics and late Cenozoic strain distribution in central and eastern Iran, *Tectonics*,
799 *23*(5), doi:10.1029/2003TC001529.
- 800 Wang, Q., P. Z. Zhang, J. T. Freymueller, R. Bilham, K. M. Larson, X. Lai, X. You, Z. Niu, J. Wu, Y. Li, J. Liu, Z. Yang, and Q. Chen
801 (2001), Present-day crustal deformation in China constrained by global positioning system measurements, *Science (New
802 York, N. Y.)*, *294*, 574–7, doi:10.1126/science.1063647.
- 803 Wang, T., J. Zhuang, T. Kato, and M. Bebbington (2013), Assessing the potential improvement in short-term earthquake forecasts from
804 incorporation of GPS data, *Geophysical Research Letters*, *40*(February), n/a–n/a, doi:10.1002/grl.50554.
- 805 Wesnousky, S. G. (2005), Active faulting in the Walker Lane, *Tectonics*, *24*(3), 1–35, doi:10.1029/2004TC001645.
- 806 Wesnousky, S. G., L. M. Jones, C. H. Scholz, and Q. Deng (1984), Historical seismicity and rates of crustal deformation along the margins
807 of the Ordos block, North China, *Bulletin of the Seismological Society of America*, *74*(5), 1767–1783.

- 808 Wesnousky, S. G., J. M. Bormann, C. Kreemer, W. C. Hammond, and J. N. Brune (2012), Neotectonics, geodesy, and seismic hazard
809 in the Northern Walker Lane of Western North America: Thirty kilometers of crustal shear and no strike-slip?, *Earth and*
810 *Planetary Science Letters*, *329-330*, 133–140, doi:10.1016/j.epsl.2012.02.018.
- 811 Wessel, P., W. H. F. Smith, R. Scharroo, J. Luis, and F. Wobbe (2013), Generic Mapping Tools: Improved Version Released, *Eos*,
812 *Transactions American Geophysical Union*, *94* (45), 409–410, doi:10.1002/2013EO450001.
- 813 Wright, T. J., J. R. Elliott, H. Wang, and I. Ryder (2013), Earthquake cycle deformation and the Moho: Implications for the rheology
814 of continental lithosphere, *Tectonophysics*, *609*, 504–523, doi:10.1016/j.tecto.2013.07.029.
- 815 Xu, X., and Q. Deng (1990), The features of late Quaternary activity of the piedmont fault of Mt. Huoshan, Shanxi province and 1303
816 Hongdong earthquake (Ms=8), *Seismology and Geology*, *12*(1), 21–32 (in Chinese).
- 817 Xu, X., and X. Ma (1992), Geodynamics of the Shanxi Rift system, China, *Tectonophysics*, *208*(1-3), 325–340, doi:
818 10.1016/0040-1951(92)90353-8.
- 819 Xu, X., Q. Deng, and H. You (1986), Evidence on dextral dislocation of fault at the western foothills of Mt. Xizhoushan, Shanxi province
820 and its slip rate during the Holocene, *Seismology and Geology*, *8*(3), 44–46 (in Chinese).
- 821 Xu, X., X. Ma, and Q. Deng (1993), Neotectonic activity along the Shanxi rift system, China, *Tectonophysics*, *219*(4), 305–325,
822 doi:10.1016/0040-1951(93)90180-R.
- 823 Xu, X., G. Cheng, X. Ma, Y. Sun, and Z. Han (1994), Rotation model and dynamics of blocks in north China and its adjacent areas,
824 *Earth Science - Journal of China University of Geosciences*, *19*(2), 129–138 (in Chinese).
- 825 Yu, S. (2004), A study on characteristics of tectonic block motion and tectonic setting of strong earthquakes in northern part of the
826 Shanxi fault depression zone, *Acta Seismologica Sinica*, *17*(4), 417–425, doi:10.1007/s11589-004-0021-5.
- 827 Yuan, D.-Y., W.-P. Ge, Z.-W. Chen, C.-Y. Li, Z.-C. Wang, H.-P. Zhang, P.-Z. Zhang, D.-W. Zheng, W.-J. Zheng, W. H. Craddock, K. E.
828 Dayem, A. R. Duvall, B. G. Hough, R. O. Lease, J.-D. Champagnac, D. W. Burbank, M. K. Clark, K. a. Farley, C. N. Garzzone,
829 E. Kirby, P. Molnar, and G. H. Roe (2013), The growth of northeastern Tibet and its relevance to large-scale continental geodynamics:
830 A review of recent studies, *Tectonics*, *32*(5), 1358–1370, doi:10.1002/tect.20081.
- 831 Zhang, B., Y. Liao, S. Guo, R. E. Wallace, R. C. Bucknam, and T. C. Hanks (1986), Fault scarps related to the 1739 earthquake and
832 seismicity of the Yinchuan Graben, Ningxia Huizu Zizhiqu, China, *Bulletin of the Seismological Society of*
833 *America*, *76*(5), 1253–1287.
- 834 Zhang, P., P. Molnar, B. C. Burchfiel, and L. Royden (1988), Bounds on the Holocene slip rate of the Haiyuan Fault, north-central
835 China, *Quaternary Research*, *30*, 151–164.
- 836 Zhang, P., B. C. Burchfiel, P. Molnar, W. Zhang, D. Jiao, Q. Deng, Y. Wang, L. Royden, and F. Song (1990), Late Cenozoic tectonic
837 evolution of the Ningxia-Hui Autonomous Region, China, *Geological Society of America Bulletin*, *102*(11),
838 1484–1498, doi:10.1130/0016-7606(1990)102;1484.
- 839 Zhang, W., D. Jiao, P. Zhang, P. Molnar, B. C. Burchfiel, Q. Deng, Y. Wang, and F. Song (1987), Displacement along the Haiyuan
840 Fault associated with the great 1920 Haiyuan, China, earthquake, *Bulletin of the Seismological Society of*
841 *America*, *77*(1), 117–131.
- 842 Zhang, Y., J. L. Mercier, and P. Vergely (1998), Extension in the graben systems around the Ordos (China), and its contribution to the
843 extrusion tectonics of south China with respect to Gobi-Mongolia, *Tectonophysics*, *285*, 41–75.
- 844 Zhang, Y. Q., P. Vergely, and J. Mercier (1995), Active faulting in and along the Qinling Range (China) inferred from SPOT imagery
845 analysis and extrusion tectonics of south China, *Tectonophysics*, *243*, 69–95.
- 846 Zhao, B., Y. Huang, C. Zhang, W. Wang, K. Tan, and R. Du (2015), Crustal deformation on the Chinese mainland during 19982014
847 based on GPS data, *Geodesy and Geodynamics*, *6*(1), 7–15, doi:10.1016/j.geog.2014.12.006.
- 848 Zheng, B., S. Guo, and H. Xu (1981), Preliminary study of principal features of the NW and NWW trending fault structures in the
849 Yanshan region, *Seismology and Geology*, *3*(2), 31–40 (in Chinese).
- 850 Zheng, D., P. Z. Zhang, J. Wan, D. Yuan, C. Li, G. Yin, G. Zhang, Z. Wang, W. Min, and J. Chen (2006), Rapid exhumation at ~ 8 Ma
851 on the Liupan Shan thrust fault from apatite fission-track thermochronology: Implications for growth of the northeastern Tibetan
852 Plateau margin, *Earth and Planetary Science Letters*, *248*(1-2), 183–193, doi:10.1016/j.epsl.2006.05.023.
- 853 Zhou, M., T. Lü, Y. Zhang, and A. Ruan (2000), The geological structure background and the crustal structure in the northeastern
854 margin of the Qinghai-Tibetan plateau, *Acta Seismologica Sinica*, *13*(6), 687–697, doi:10.1007/s11589-000-0071-2.
- 855 Zhou, Y., B. Parsons, J. R. Elliott, I. Barisin, and R. T. Walker (2015), Assessing the ability of Pleiades stereo imagery to determine height
856 changes in earthquakes: A case study for the El Mayor-Cuapah epicentral area, *Journal of Geophysical Research*
857 *(Solid Earth)*, *120*, 8793–8808, doi:10.1002/2015JB012358.Received.

Table 1. Lateral offset measurements on the Luoshan Fault^a

Feature	Latitude / °	Longitude / °	Lateral offset / m
<i>Xiaoluoshan</i>			
Thalweg	37.1840	106.3353	30.2
Thalweg	37.1826	106.3358	41.2
Riser top	37.1816	106.3361	29.2
Riser top	37.1811	106.3364	33.1
Riser top	37.1790	106.3374	40.2
Riser bottom	37.1789	106.3374	44.4
Riser top	37.1775	106.3379	35.2
Riser top	37.1766	106.3381	39.7
Riser top	37.1760	106.3384	42.0
			37.2 ± 5.5^b
<i>Tanzhuangzicun</i>			
Riser top	37.4266	106.2793	57.0
Riser bottom	37.4263	106.2793	54.5
Riser top	37.4261	106.2793	61.4
Riser top	37.4232	106.2799	47.5
Riser top	37.4228	106.2799	48.0
Riser top	37.4173	106.2806	50.9
Riser top	37.4168	106.2806	45.8
Thalweg	37.4146	106.2810	50.1
Riser top	37.4120	106.2814	37.2
Riser top	37.4117	106.2814	54.0
			50.6 ± 6.7^c
<i>Shiyaodong</i>			
Thalweg	37.2521	106.3201	33.8
Thalweg	37.2508	106.3203	48.5
Thalweg	37.2493	106.3205	44.5
Thalweg	37.2483	106.3204	41.9
Thalweg	37.2466	106.3201	36.9
			41.1 ± 5.9^d

^a Latitudes and longitudes are for the intersection of the western piercing line with the mapped fault trace.

^b Mean offset and standard deviation for the Xiaoluoshan section.

^c Mean offset and standard deviation for the Tanzhuangzicun section.

^d Mean offset and standard deviation for the Shiyaodong section, re-measured after *Min et al.* [2003].

Table 2. IRSL dating results

Location	Name	Lat °	Long °	Elevation m	Depth m	Equivalent Dose Gy	Dose Rate mGy a ⁻¹	Age ^a ka
Xiaoluoshan Fault	1	106.3350	37.1850	1761	2.1			141±12
Xiaoluoshan Fault	2	106.3397	37.1780	1766	0.55			9.16±0.57
Daluoshan Fault	3	106.2800	37.4250	1422	1.7			10.6±0.9
East Helanshan Fault	4	106.6575	39.2360	1374	0.54			1.27±0.14
East Helanshan Fault	5	106.6575	39.2360	1374	1.3			3.21±0.21

^a Including 1 σ analytical uncertainties.

Table 3. Calculated slip rates and throw rates

Location	Sample No.	Latitude °	Longitude °	Age ka	Error ka	Horizontal Offset m	Error m	Slip rate mm/a	Error mm/a
<i>Luoshan Fault</i>									
Xiaoluoshan	IRSL 1	37.1850	106.3350	141	12	37.2	5.5	0.26	0.05
Xiaoluoshan	IRSL 2	37.1780	106.3397	9.16	0.57	37.2	5.5	4.1	0.7
Tanzhuangzicun	IRSL 3	37.4250	106.2800	10.6	0.9	50.6	6.7	4.8	0.8
Shiyaodong ^a	TL	37.2519	106.3204	9.80	0.75	41.1	5.9	4.2	0.7
Average^b								4.3	0.4^c
<i>East Helanshan Fault</i>									
Northern end of fault	IRSL 4	39.2360	106.6575	1.27	0.14	16.0	5.0	12.6	4.2
Northern end of fault	IRSL 5	39.2360	106.6575	3.21	0.21	16.0	5.0	5.0	1.6
Location	Sample No.	Latitude deg	Longitude deg	Age ka	Error ka	Vertical Offset m	Error m	Throw rate mm/a	Error mm/a
<i>East Helanshan Fault</i>									
Suyukou scarps, T5	STM10 ^d	38.7839	106.1343	221.5	3.9	19.4	1.1	0.09	0.01
Suyukou scarps, T5	STM10 ^e	38.7839	106.1343	157.2	4.1	19.4	1.1	0.12	0.01
Central Suyukou scarps	STM15 ^f	38.7063	106.0270	32.7	1.1	11.2	1.5	0.34	0.05
Helanshan range-front	STM9	38.7359	106.0117	120.6	1.9	24.0	4.0	0.20	0.03
Helanshan range-front	STM9 ^g	38.7359	106.0117	56.3	2.2	24.0	4.0	0.43	0.07
Sum^h								0.8	0.1
Extension rateⁱ								0.9	0.1

^a Re-assessment of the data from Shiyaodong [*Min et al.*, 2003].^b Error-weighted average of samples IRSL 2, IRSL 3 and TL.^c Error is the weighted standard deviation of the three slip rate estimates.^d Assuming a zero inheritance model.^e Corrected for inheritance by subtracting STM13A.^f Corrected for inheritance by subtracting STM16C.^g Corrected for inheritance by subtracting STM13A.^h Sum of 0.34 and 0.43 mm/a for parallel Suyukou and range-front strands.ⁱ Assuming the smallest fault dip found in the literature of 39° from *Fang et al.* [2009].

Table 4. ^{10}Be dating results

Location	Name	Type ^a	Lat °	Long °	Elevation m	Thickness cm	Density g cm ⁻³	Shielding factor	[¹⁰ Be] ^b 10 ³ atoms g ⁻¹	Exposure age ^c / ka
Range-front terrace	STM9	A	38.7359	106.0117	1461	2	2.65	0.9628	1498.0±22.7	120.6±1.9
Range-front terrace	STM1	B	38.7363	106.0111	1486	3	2.70	0.9674	1409.0±24.7	111.5±2.0
Range-front fan	STM3	B	38.7354	106.0143	1414	3	2.65	0.9832	206.2±7.0	16.5±0.6
Range-front fan	STM4	B	38.7353	106.0138	1413	3	2.73	0.9832	163.5±11.4	13.1±0.9
Range-front fan	STM5	B	38.7354	106.0138	1411	3	2.75	0.9832	101.9±13.3	8.2±1.1
Range-front fan	STM6	B	38.7354	106.0138	1419	3	2.73	0.9832	138.7±6.5	11.1±0.5
Range-front fan	STM7	B	38.7349	106.0149	1400	3	2.73	0.9795	219.0±6.7	17.8±0.6
Range-front fan	STM8	B	38.7344	106.0150	1399	3	2.74	0.9795	469.0±16.4	38.3±1.4
T5	STM10	A	38.7839	106.1343	1193	2	2.67	0.9996	2288.0±38.3	221.5±3.9
T5	STM11A	C	38.7828	106.1398	1162	4	2.65	0.9996	1560.6±32.5	154.4±3.3
T5	STM11B	C	38.7828	106.1398	1162	4	2.65	0.9996	2161.5±29.8	217.0±3.2
T5	STM11C	C	38.7828	106.1398	1162	4	2.65	0.9996	2094.9±23.4	209.6±2.5
T5	STM11D	C	38.7828	106.1398	1162	4	2.65	0.9996	1084.5±17.0	105.6±1.7
T5	STM11E	C	38.7828	106.1398	1162	4	2.65	0.9996	1820.7±43.3	181.3±4.5
T5	STM11F	C	38.7828	106.1398	1162	4	2.65	0.9996	2215.7±23.4	223.4±2.5
T5	STM11G	C	38.7828	106.1398	1162	4	2.65	0.9996	2134.5±36.8	213.9±3.9
T5	STM11H	C	38.7828	106.1398	1162	4	2.65	0.9996	2054.8±46.8	205.4±4.9
T5 (inheritance)	STM12	A	38.7766	106.1285	1194	2	2.67	0.9996	299.0±7.5	27.5±0.7
T5 (inheritance)	STM13A	C	38.7766	106.1285	1194	4	2.68	0.9996	679.6±12.2	64.3±1.2
T5 (inheritance)	STM13B	C	38.7766	106.1285	1194	4	2.68	0.9996	85.4±3.8	8.1±0.4
T2	STM14	A	38.7047	106.0248	1254	2	2.66	0.9993	209.9±5.5	18.5±0.5
T2	STM14A	C	38.7047	106.0248	1254	4	2.66	0.9993	96.9±3.6	8.9±0.3
T2	STM14B	C	38.7047	106.0248	1254	4	2.66	0.9993	859.5±16.2	78.0±1.5
T2	STM14C	C	38.7047	106.0248	1254	4	2.66	0.9993	110.4±7.7	9.8±0.7
T3	STM15	A	38.7063	106.0270	1251	2	2.67	0.9993	475.7±11.5	42.3±1.0
T2 & T3 (inheritance)	STM16	A	38.7080	106.0330	1264	2	2.69	0.9993	165.0±8.0	14.4±0.7
T2 & T3 (inheritance)	STM16A	C	38.7080	106.0330	1264	5	2.69	0.9993	108.3±3.3	9.7±0.3
T2 & T3 (inheritance)	STM16B	C	38.7080	106.0330	1264	5	2.69	0.9993	226.1±5.4	20.3±0.5
T2 & T3 (inheritance)	STM16C	C	38.7080	106.0330	1264	5	2.69	0.9993	107.4±3.7	9.6±0.3
T2 & T3 (inheritance)	STM16D	C	38.7080	106.0330	1264	5	2.69	0.9993	373.8±8.3	33.6±0.8

^a A = aggregate of pebbles; B = boulder top; C = clast

^b Background corrected values. Errors are analytical AMS uncertainties for samples and blanks propagated in quadrature. The NIST_27900 standard, with a ratio of 2.79×10^{-11} was used for all samples.

^c Exposure ages were calculated with the CRONUS-Earth online calculator (version 2.2), using a constant production rate model and a sea-level high-latitude reference production rate of 4.49 ± 0.39 atoms g⁻¹ yr⁻¹ [Lal, 1991; Stone, 2000; Balco et al., 2008].

D R A F T

March 22, 2016, 4:55pm

D R A F T

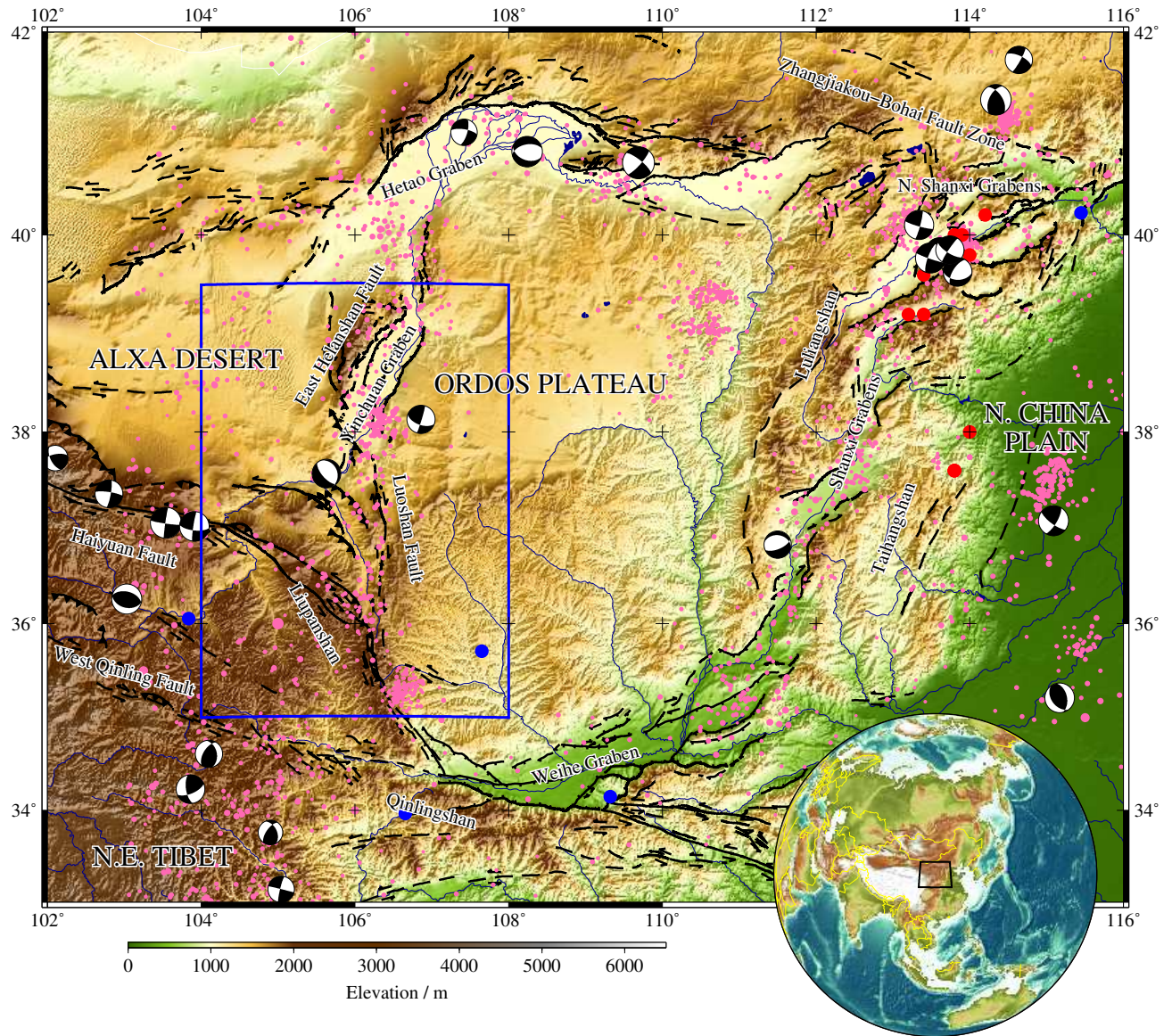


Figure 1. SRTM topography of the Ordos Plateau in northeastern China [Farr *et al.*, 2007]. Focal mechanisms from the Global CMT catalogue [Ekström *et al.*, 2012] are shown for recent earthquakes (1976 to present) with magnitudes greater than M_w 5.0. Earthquakes of M_w 2.0-5.0 since 1920 from the ISC catalogue [International Seismological Centre, 2013] are shown as pink dots. Faults, marked as thin black lines, have been mapped from satellite imagery (source: <http://earth.google.com>) based upon earlier fault maps from Tapponnier and Molnar [1977], Deng *et al.* [1984], Zhang *et al.* [1986], Zhang *et al.* [1990], Xu and Ma [1992], Deng and Liao [1996], Darby and Ritts [2002], Yu [2004] and Darby *et al.* [2005]. Faults that are inferred or show no clear evidence of Quaternary activity are marked by dashed lines. Red dots show locations of palaeomagnetism samples used by Xu *et al.* [1994]; blue dots show locations of palaeomagnetism samples used by Li *et al.* [2001]. Rivers are indicated in dark blue. The blue polygon indicates the region shown in Figure 3.

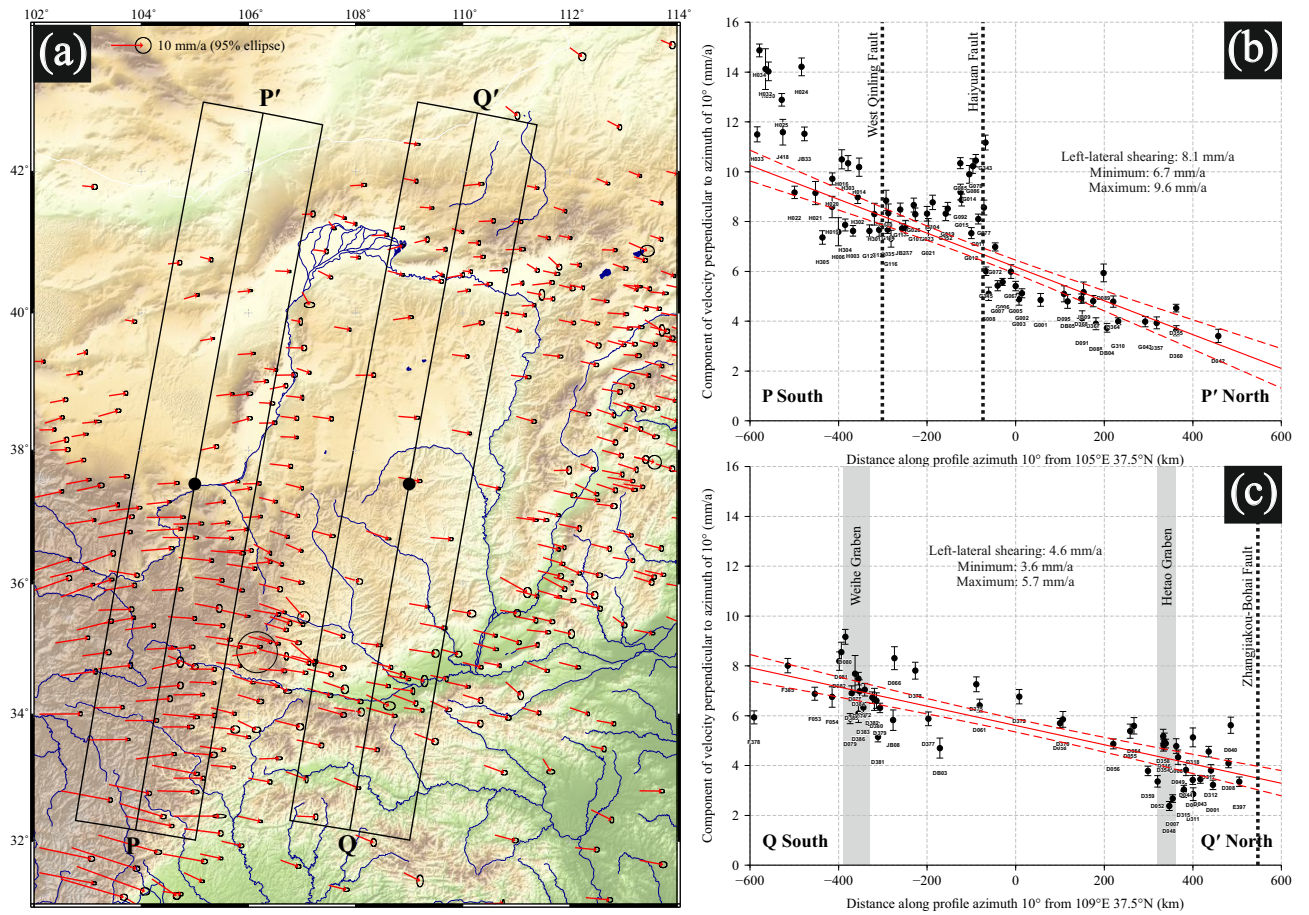


Figure 2. (a) SRTM topography of the Ordos Plateau in northeastern China [Farr *et al.*, 2007]. Red arrows show campaign GPS measurements made over a period of 4 years (occupations in 2009, 2011 and 2013) from Zhao *et al.* [2015] relative to stable Eurasia. (b) Swath profile through the GPS data west of the Ordos Plateau showing the velocity component perpendicular to the profile. The red line is the best fit least squares regression to the data and the dashed red lines are the 95% confidence envelopes on this best fit line. The profile shows left-lateral shear of 8.1 ± 1.5 mm/a averaged over the extent of the profile—with approximately 5 mm/a being taken up on the Haiyuan Fault. (c) Same as (b), but for a swath profile through the centre of the Ordos Plateau, showing left-lateral shear of 4.6 ± 1.1 mm/a averaged over the extent of the profile—though it does not appear to be localised on any one individual structure. The difference between the two profiles is potentially due to absorption of some of the eastward motion in the Liupanshan thrust belt.

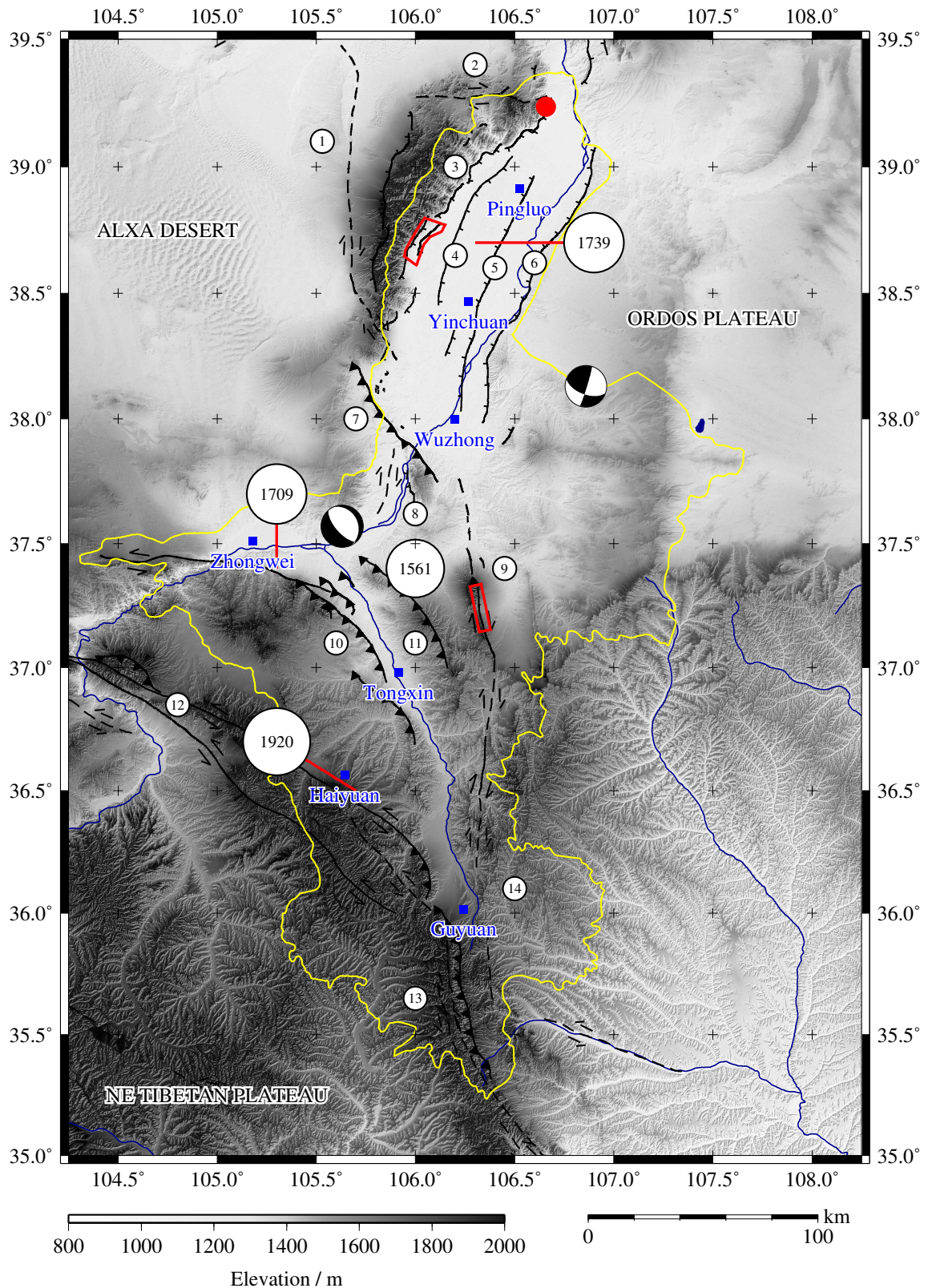


Figure 3. SRTM topography (30 m resolution) of the study area in the western Ordos region, Ningxia Province, northern China [Farr *et al.*, 2007]. The province is outlined in yellow and cities are marked by blue squares. Focal mechanisms are from the Global CMT catalogue [Ekström *et al.*, 2012]. Major historical earthquakes are shown by white circles, including the year in which they occurred [Liu *et al.*, 2011]. Red outlines indicate coverage of Pleiades data. Red circle indicates field site at the northern end of the East Helanshan Fault (see Figure 15). Faults, marked as thin black lines, have been mapped from satellite imagery (source: <http://earth.google.com>) based upon earlier fault maps from Tapponnier and Molnar [1977], Deng *et al.* [1984], Zhang *et al.* [1990], Darby and Ritts [2002] and Darby *et al.* [2005]. Faults that are inferred or show no clear evidence of Quaternary activity are marked by dashed lines. Faults are numbered as follows (slip rates, where given are LL = left-lateral, RL = right-lateral and V = vertical): 1 Alxa Desert Fault; 2 Zhengyiguan Fault; 3 East Helanshan Fault, 0.5-0.8 mm/a V; 4 Luhutai Fault; 5 Yinchuan-Pingluo Fault; 6 Yellow River (Huang He) Fault, 0.23-0.25 mm/a V; 7 Niushoushan Fault; 8 Baima Fault; 9 Luoshan Fault, 2.15 ± 0.20 mm/a RL; 10 Tianjinshan-Miboshan (Zhongwei-Tongxin) Fault, 1.5-4.5 mm/a LL; 11 Yantongshan Fault; 12 Haiyuan Fault, 5-10 mm/a LL; 13 Liupanshan Fault; 14 Yunwushan Fault [Zhang *et al.*, 1990; Min *et al.*, 2000, 2003; Deng *et al.*, 2004; Li *et al.*, 2013]

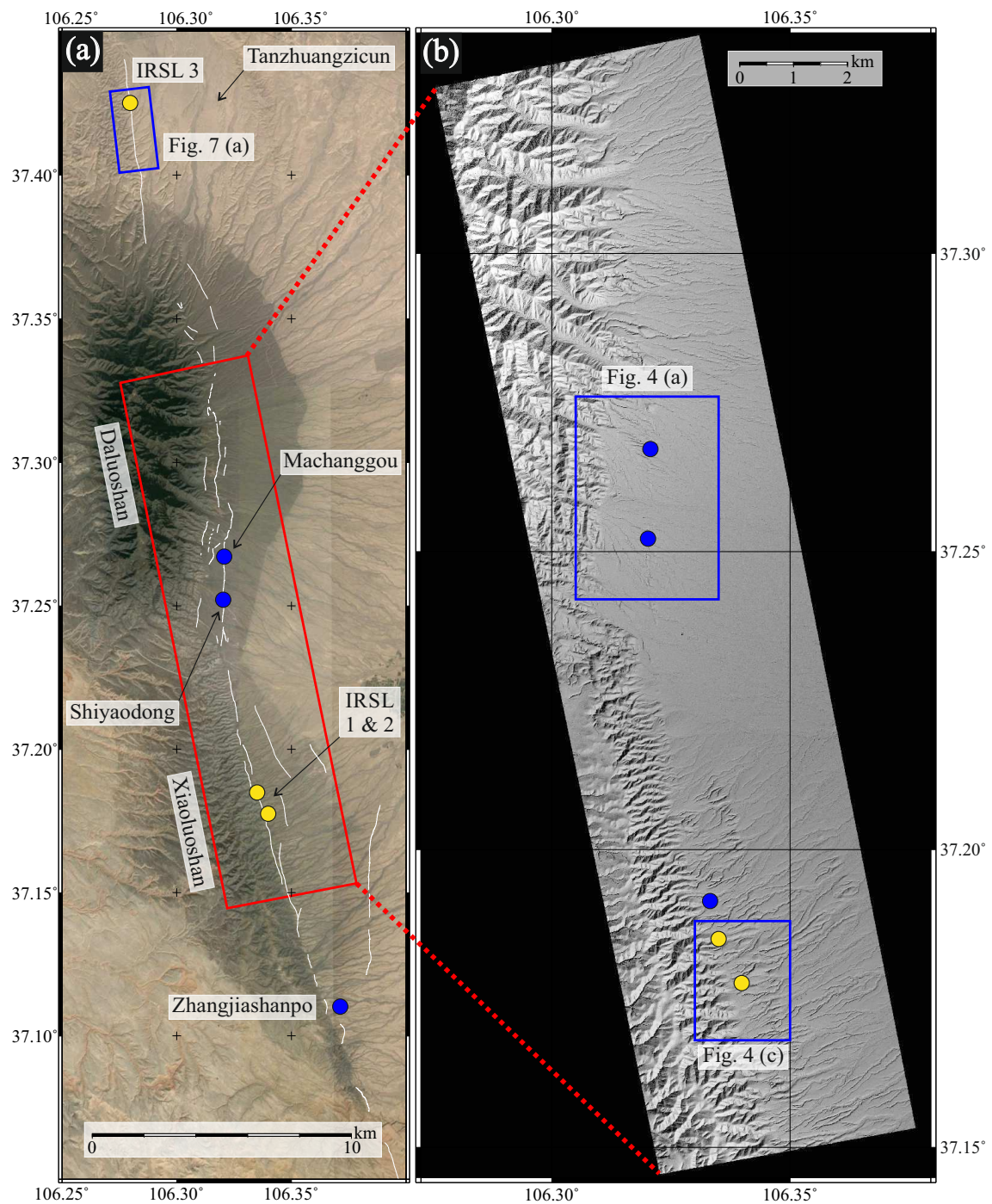


Figure 4. (a) Google Earth imagery from April and December 2013 (source: <http://earth.google.com>) of the Luoshan Fault with fault scarps mapped in white. Slip rate sites in this study are marked by yellow dots; sites from *Min et al.* [2003] are marked by blue dots. Red polygon shows coverage of Pleiades data. (b) Pleiades DEM of the central portion of the Luoshan Fault. Blue polygons show locations of other figures.

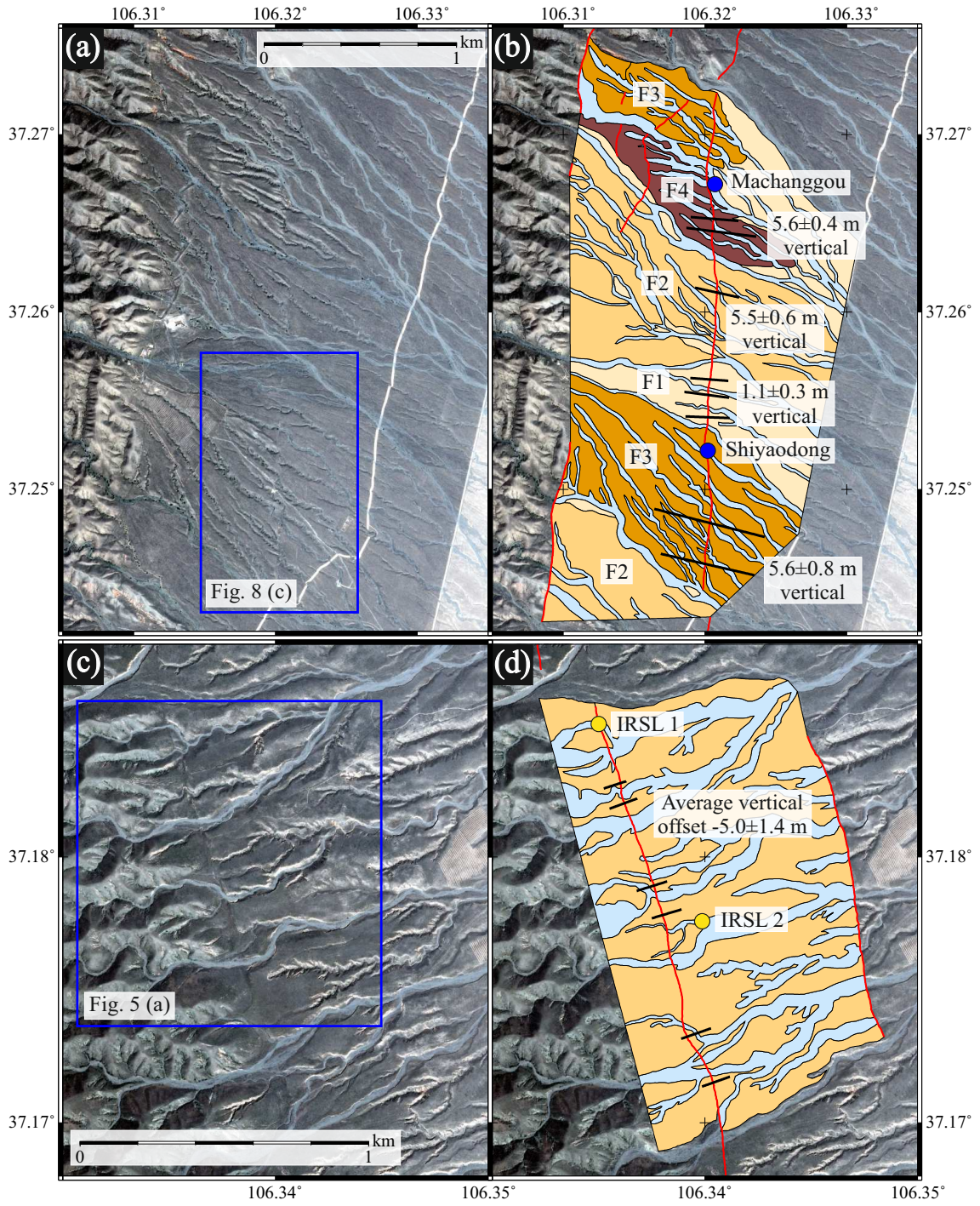


Figure 5. (a) Zoom of the Pleiades imagery in the vicinity of the slip rate sites used by *Min et al.* [2003]. (b) Annotated version of (a) with alluvial surfaces of different ages shown in different shades of brown and fault scarps mapped in red. Black lines indicate locations of topographic profiles used to estimate vertical offset preserved by each fan surface. (c) Zoom of the Pleiades imagery in the vicinity of the slip rate sites used in this study. Blue polygon shows location of Figure 6 (a). (d) Annotated version of (c). Black lines indicate locations of topographic profiles used to estimate average vertical offset preserved by this alluvial surface.

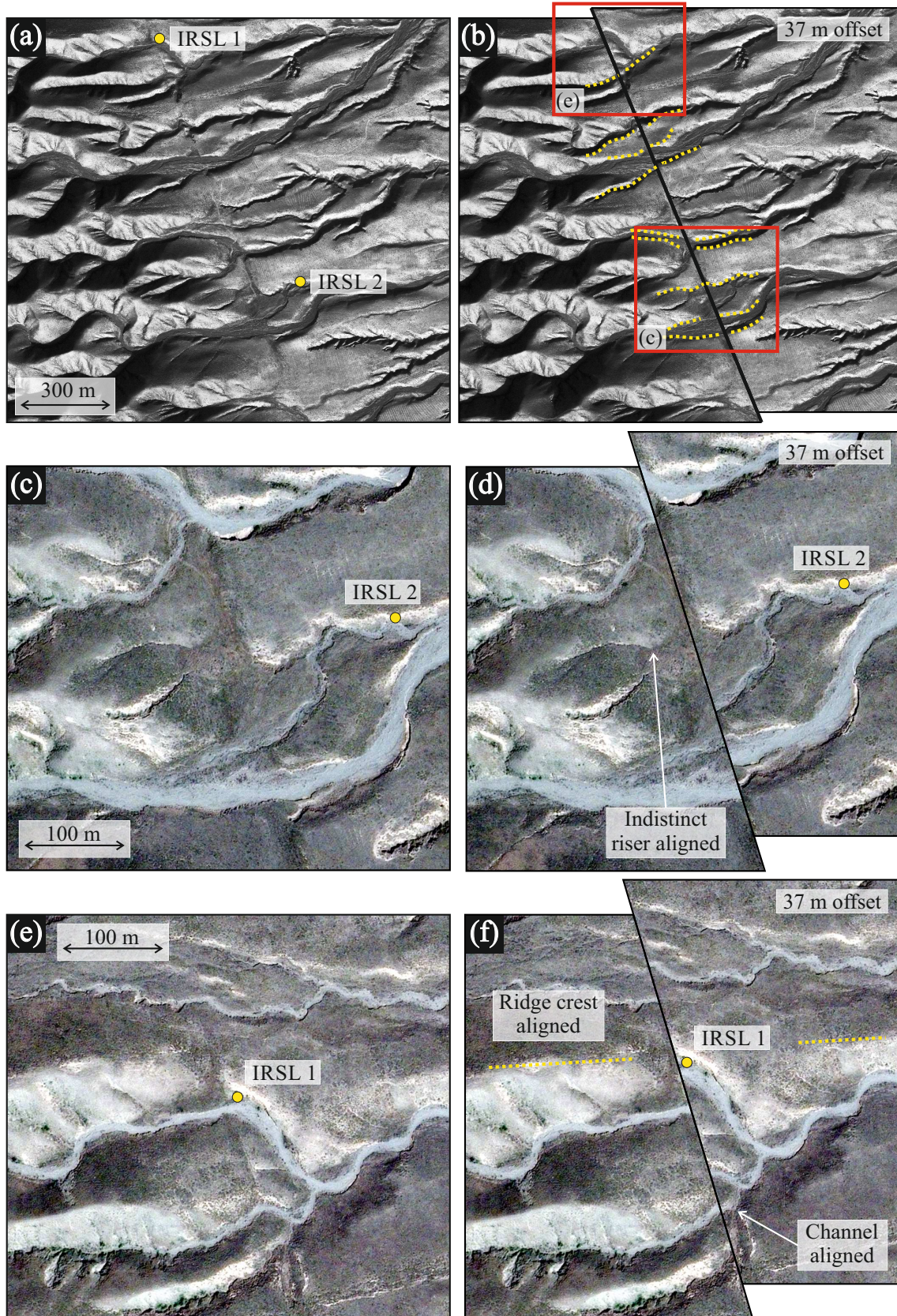


Figure 6. (a) 0.5 m resolution Worldview imagery showing a section of the Luoshan Fault adjacent to the Xiaoluoshan (see Figure 5 for precise location). The fault cuts across the image from north-northwest to south-southeast. The locations of IRSL samples 1 and 2 are indicated by yellow circles. (b) 37 m restoration, aligning various channel thalwegs and terrace risers (highlighted in yellow). Red boxes indicate locations of figures below. (c) 0.5 m resolution Pleiades imagery of the region marked in (b) and showing the location of IRSL sample 2. (d) Same as (c) with a 37 m restoration, aligning the sampled terrace riser. (e) 0.5 m resolution Pleiades imagery of the region marked in (b) and showing the location of IRSL sample 1. (d) Same as (e) with a 37 m restoration, aligning the channel thalweg to the south of the image and the ridge crest adjacent to the sampling site.

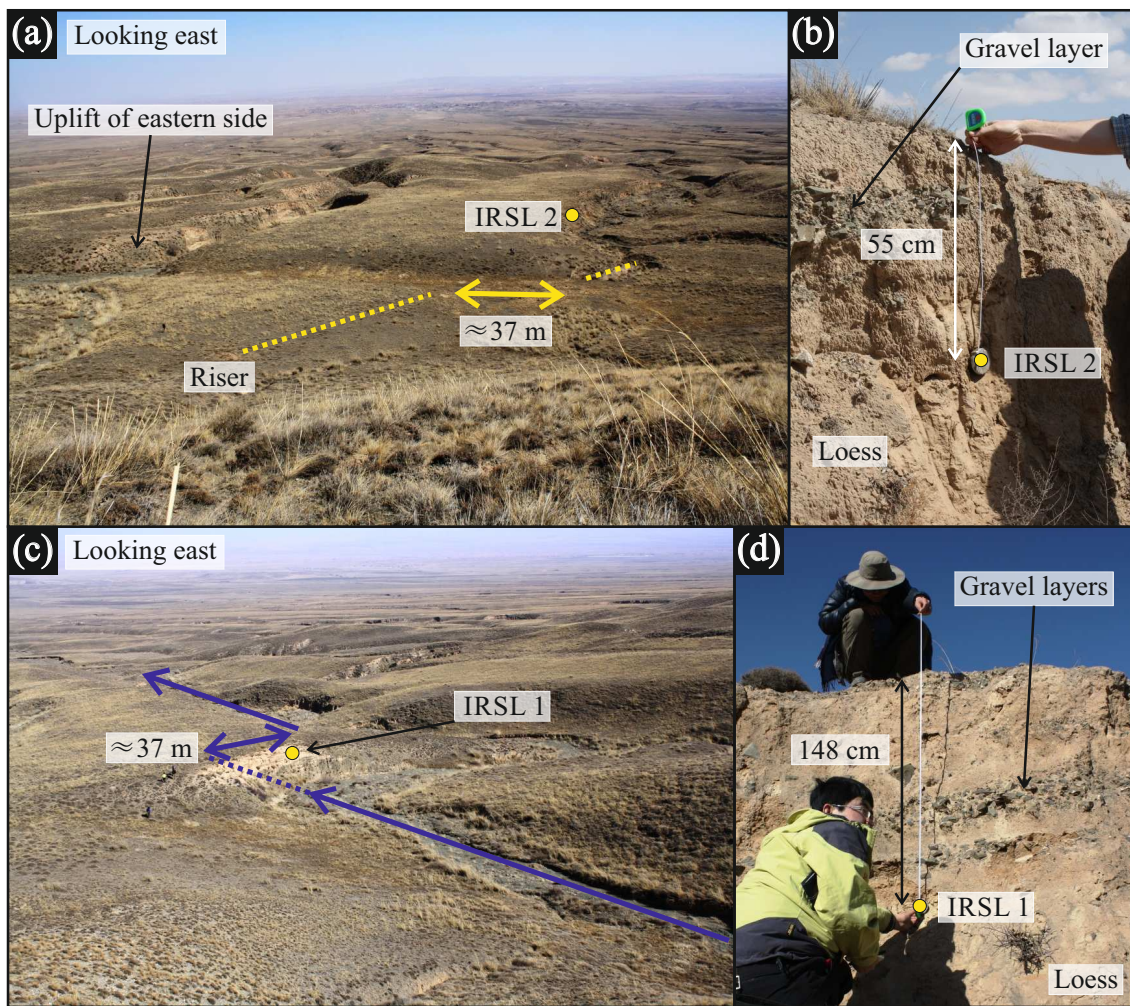


Figure 7. (a) Field photograph (taken at 37.178°N , 106.340°E) showing an overview of IRSL sample site 2. A riser on the western side of the fault trace, highlighted in yellow, can be identified by a change in the grass-cover. (b) Close-up field photograph showing the sedimentary context of IRSL sample 2. (c) Field photograph (taken at 37.185°N , 106.335°E) showing an overview of IRSL sample site 1. There is a large meander in the stream at the location of the fault trace, but the far-field offset is of the order of 37 m. (d) Close-up field photograph showing the sedimentary context of IRSL sample 1.

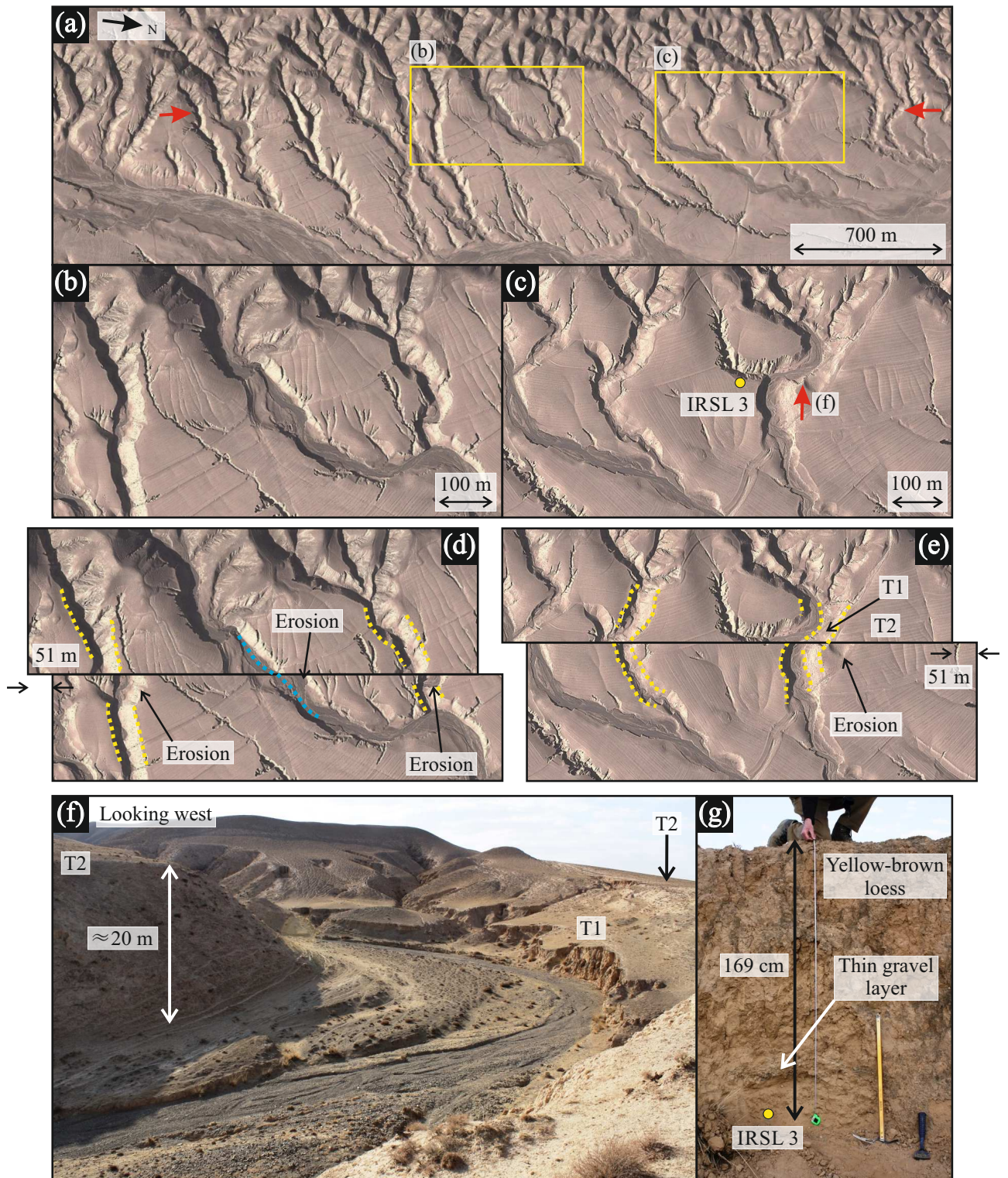


Figure 8. (a) Google Earth imagery from December 2013 (source: <http://earth.google.com>) of the Luoshan Fault north of the Daluoshan and around 1.75 km west of the village of Tanzhuangzicun (see Figure 4 (a) for precise location). Fault location is marked by red arrows. (b) Zoomed in view of the Google Earth imagery at the location marked in (a). (c) Zoomed in view of the Google Earth imagery at the location marked in (a). The location of IRSL sample 3 (at 37.425°N , 106.280°E) is indicated by the yellow circle. (d) Restoration of (b) indicating 51 m of right-lateral offset. Aligned channel risers are highlighted in yellow and an aligned channel thalweg is shown in blue. Eroded corners of channel margins on down-slope (i.e. northern) side are also indicated. (e) Restoration of (c) indicating 51 m of right-lateral offset. Yellow lines highlight alignment of two channel risers. (f) Field photograph (taken at the location indicated in (c) showing the two terrace levels adjacent to this channel. (g) Field photograph showing the sedimentary context of IRSL sample 3.

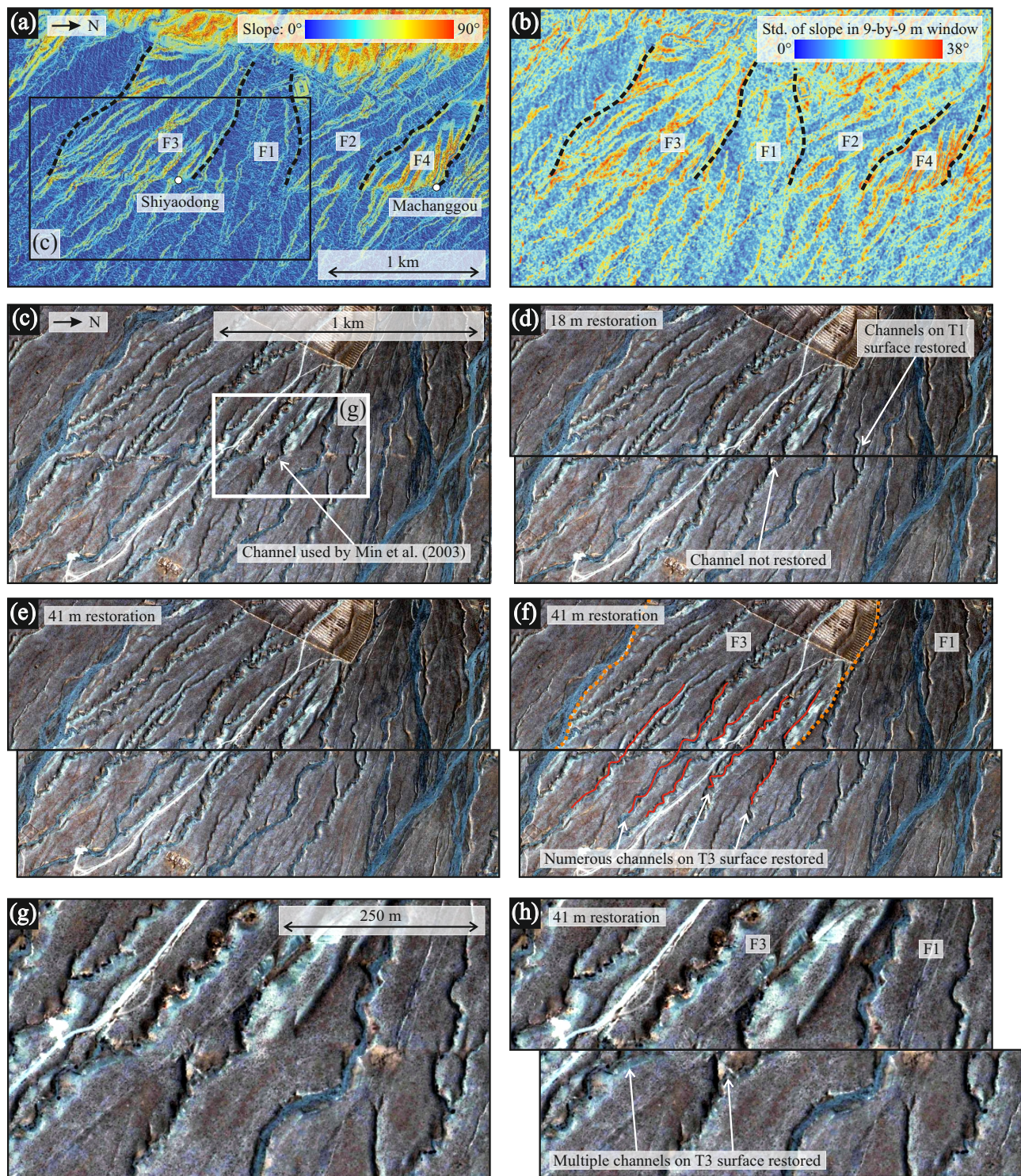


Figure 9. (a) Slope map derived from the Pleiades DEM. Region covered is the same as in Figure 5 (a). White dots show location of slip rate sites used by *Min et al.* [2003]. (b) Surface roughness map of the same area derived from the Pleiades DEM by taking the standard deviation of the slope of the DEM in a 9×9 m moving window [*Frankel and Dolan, 2007*]. (c) Pleiades imagery of the Shiyadong site from *Min et al.* [2003] indicating the gully used for their slip rate estimate. (d) 18 m reconstruction, showing that gullies on the F1 surface are restored, but not those on the F3 surface. (e) 41 m reconstruction, which properly aligns gullies on the F3 surface. (f) Annotated version of (e) showing that multiple channels on the F3 surface can be restored with 41 m of right-lateral slip. (g) Zoomed in view of the gullies on the F3 and F1 surfaces at the location marked in (c). (h) Zoomed in view of the 41 m restoration.

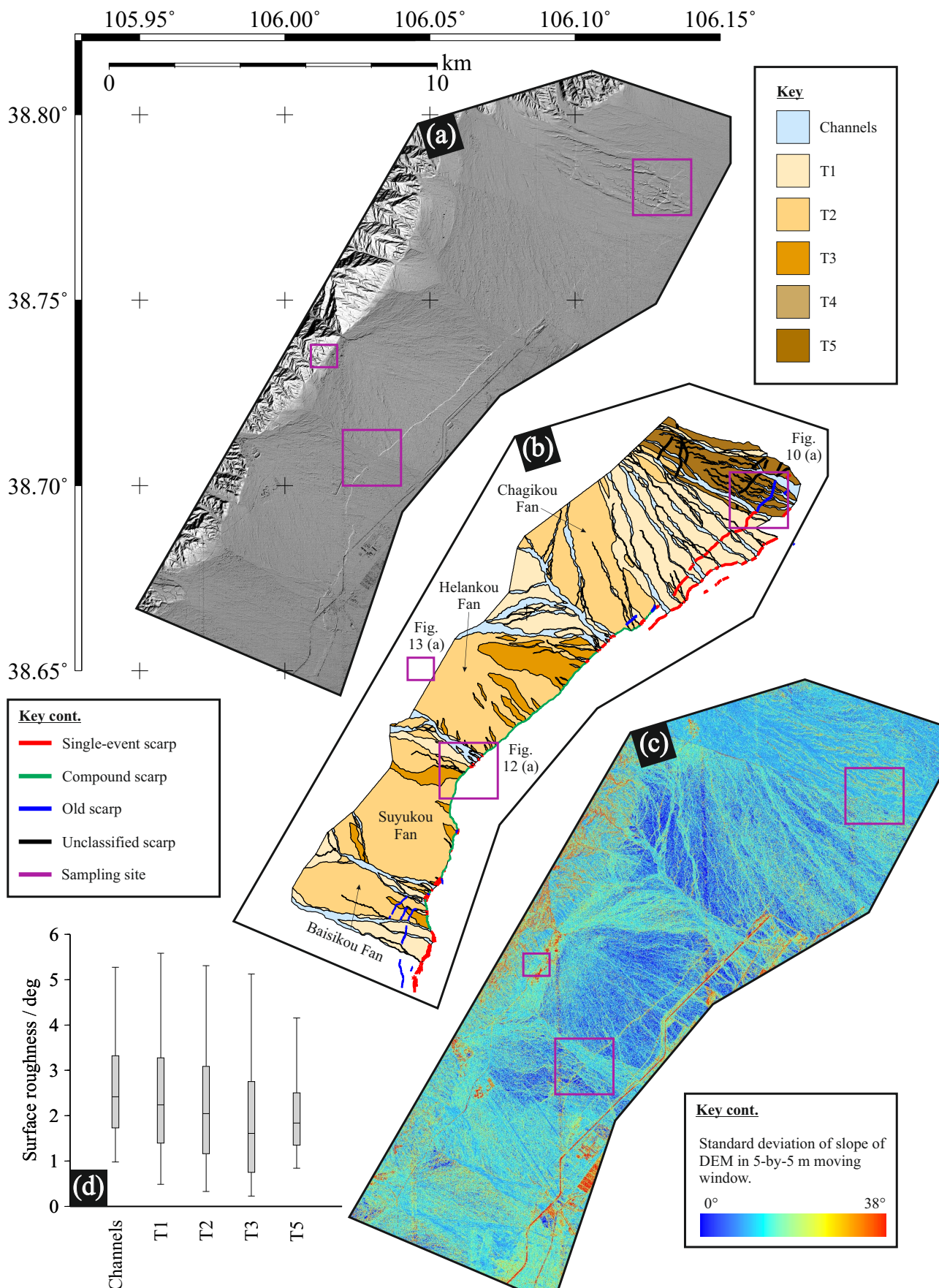


Figure 10. (a) Pleiades DEM for the Suyukou scarps at the southern end of the East Helanshan Fault. (b) Interpreted tectonic geomorphology for the Suyukou scarps at the southern end of the East Helanshan Fault. Purple polygons indicate the locations of ^{10}Be sampling sites, as shown in Figure 13. (c) Surface roughness map derived from the Pleiades DEM by taking the standard deviation of the slope of the DEM in a 5×5 m moving window [*Frankel and Dolan, 2007*]. (d) Box-and-whisker plot of the surface roughness for each alluvial unit. The horizontal bar inside each box is the median roughness; the ends of the boxes are the 25th and 75th percentiles; and the whiskers indicate the 5th and 95th percentiles.

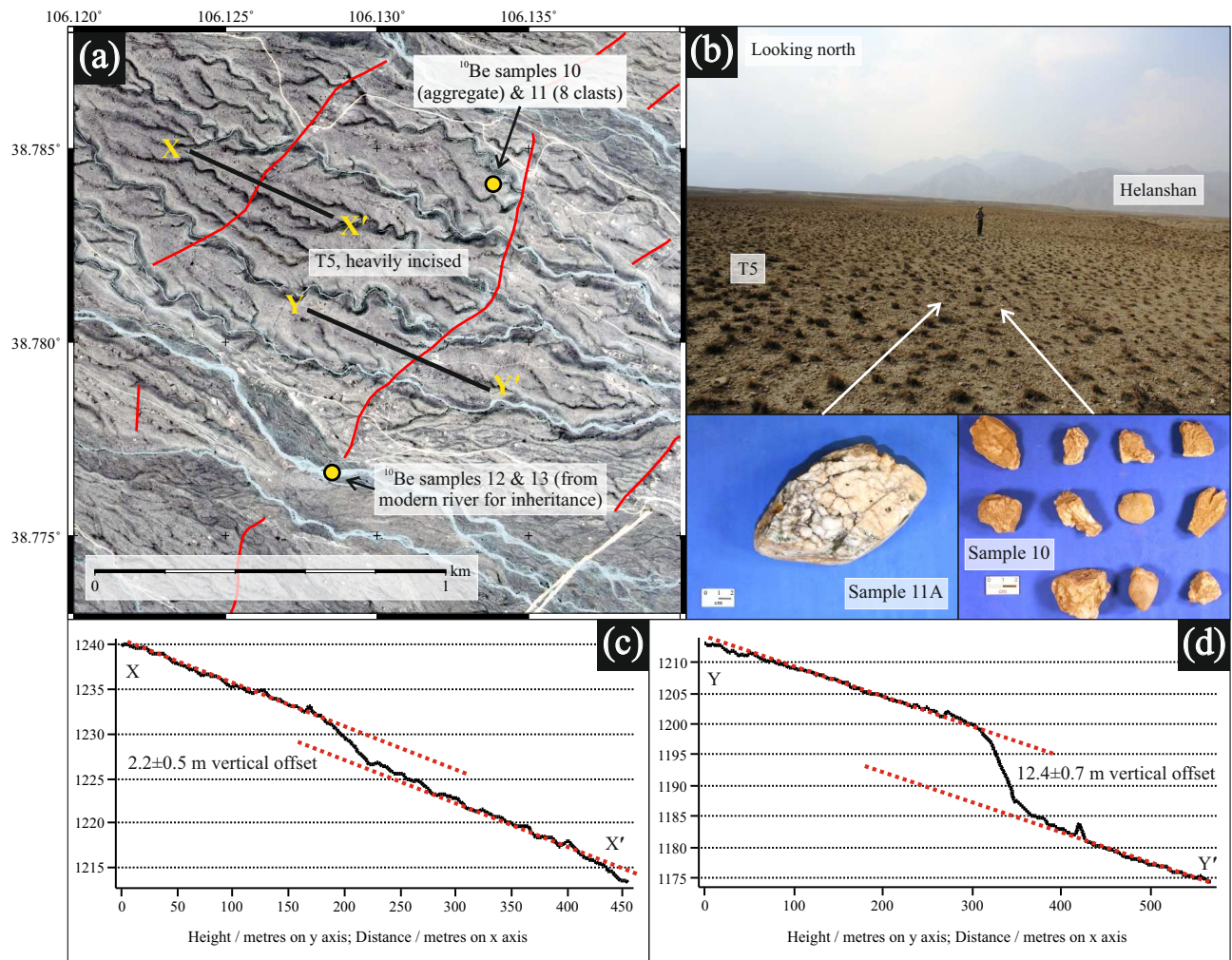


Figure 11. (a) Pleiades imagery showing the heavily incised T5 alluvial surface at the northern end of the Suyukou scarps. Fault traces are marked in red and ^{10}Be sample locations are shown by yellow circles. (b) Field photograph (taken at 38.784°N , 106.134°E) of the T5 surface. Inset photographs show quartz pebbles collected from this surface for ^{10}Be dating. (c) Topographic profile along the line X-X' in (a), showing the vertical offset on one fault strand. (d) Topographic profile along the line Y-Y' in (a), showing the vertical offset on another fault strand. Note that two other minor fault strands also offset T5 further to the northwest, giving a combined offset of 19.4 ± 1.1 m.

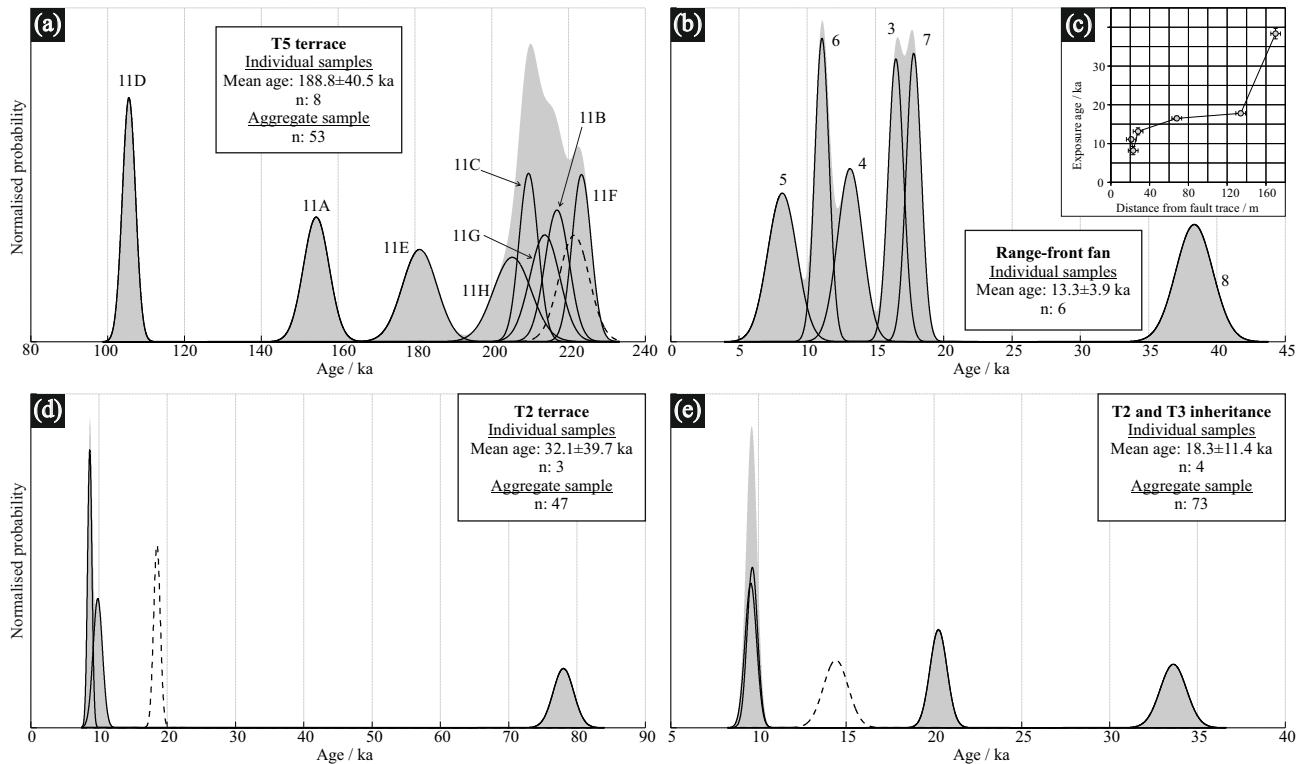


Figure 12. ^{10}Be age results for (a) T5, (b) the range-front fan, (d) T2, and (e) the T2 and T3 inheritance. Black curves are normally distributed probability density functions (PDFs) for individual samples, defined by the age and the 1σ analytical error. Grey curves are normal kernel density estimates (or camel plots), obtained by summing the individual PDFs. Dashed black curves are normally distributed PDFs for aggregate samples. (c) Plot of ^{10}Be exposure age for boulder top samples from the range-front fan against their distance from the fault trace. Error bars show 1σ analytical error on age measurements and an assumed error of ± 5 m on the distance measurements.

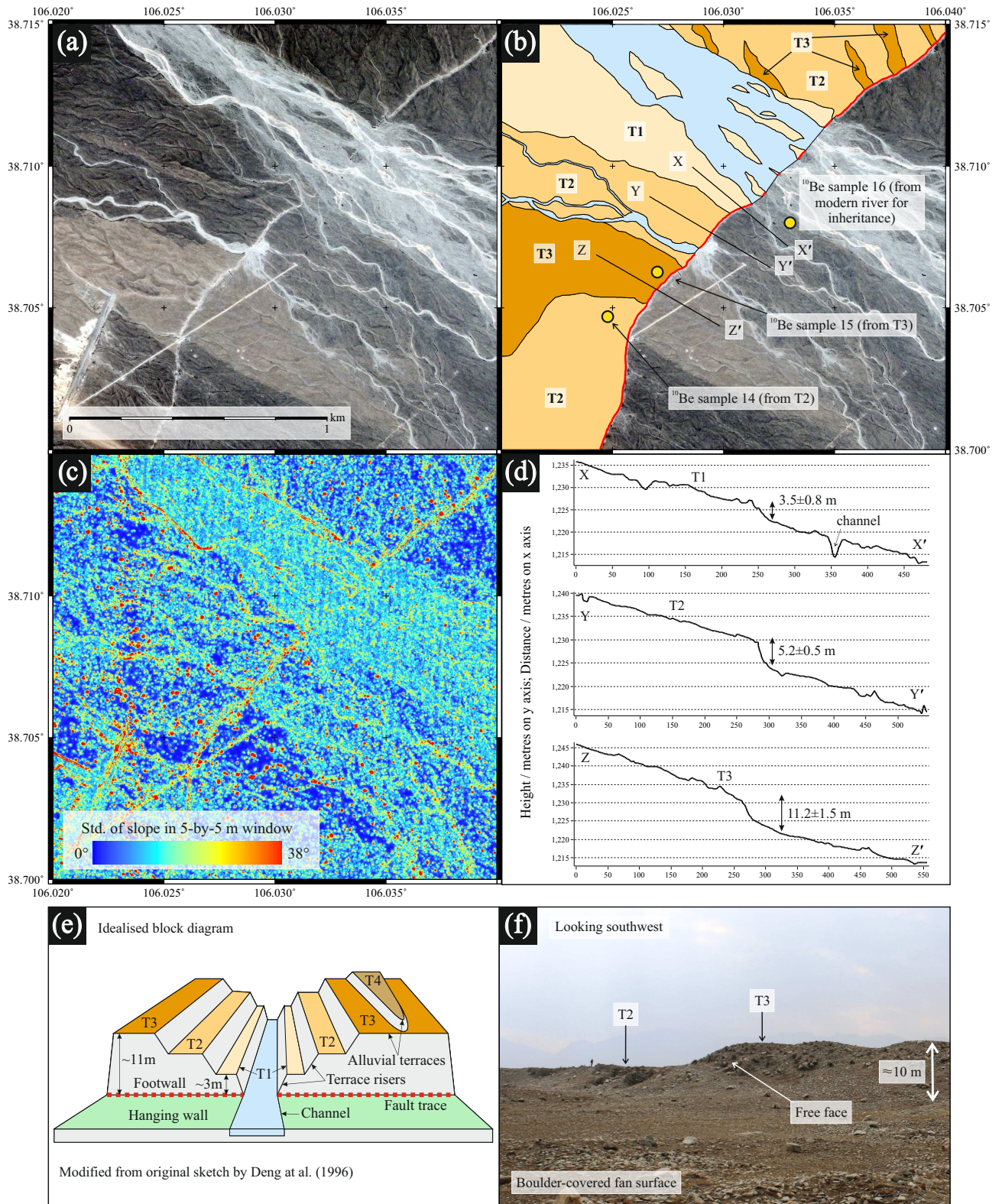


Figure 13. (a) Pleiades imagery showing an anastomosing river channel crossing the Suyukou scarps. (b) Annotated version of (a) showing mapped alluvial terrace surfaces, fault trace (in red), and ^{10}Be sample locations (yellow circles). The locations of profiles X-X', Y-Y', and Z-Z' are also indicated. (c) Surface roughness map derived from the Pleiades DEM by taking the standard deviation of the slope of the DEM in a 5×5 m moving window [Frankel and Dolan, 2007]. A number of the terraces mapped in (b) are visible in this image. (d) Three topographic profiles along the lines X-X', Y-Y', and Z-Z' at the locations shown in (b). The three profiles show typical scarp heights for representative T1, T2, and T3 alluvial terrace surfaces. (e) Idealised block diagram showing the expected preservation of aggradational alluvial terraces in the footwall of a normal fault over multiple earthquake cycles. Modified from Deng and Liao [1996]. (f) Field photograph (taken at 38.706°N , 106.028°E) of the Suyukou scarps showing T2 and T3.

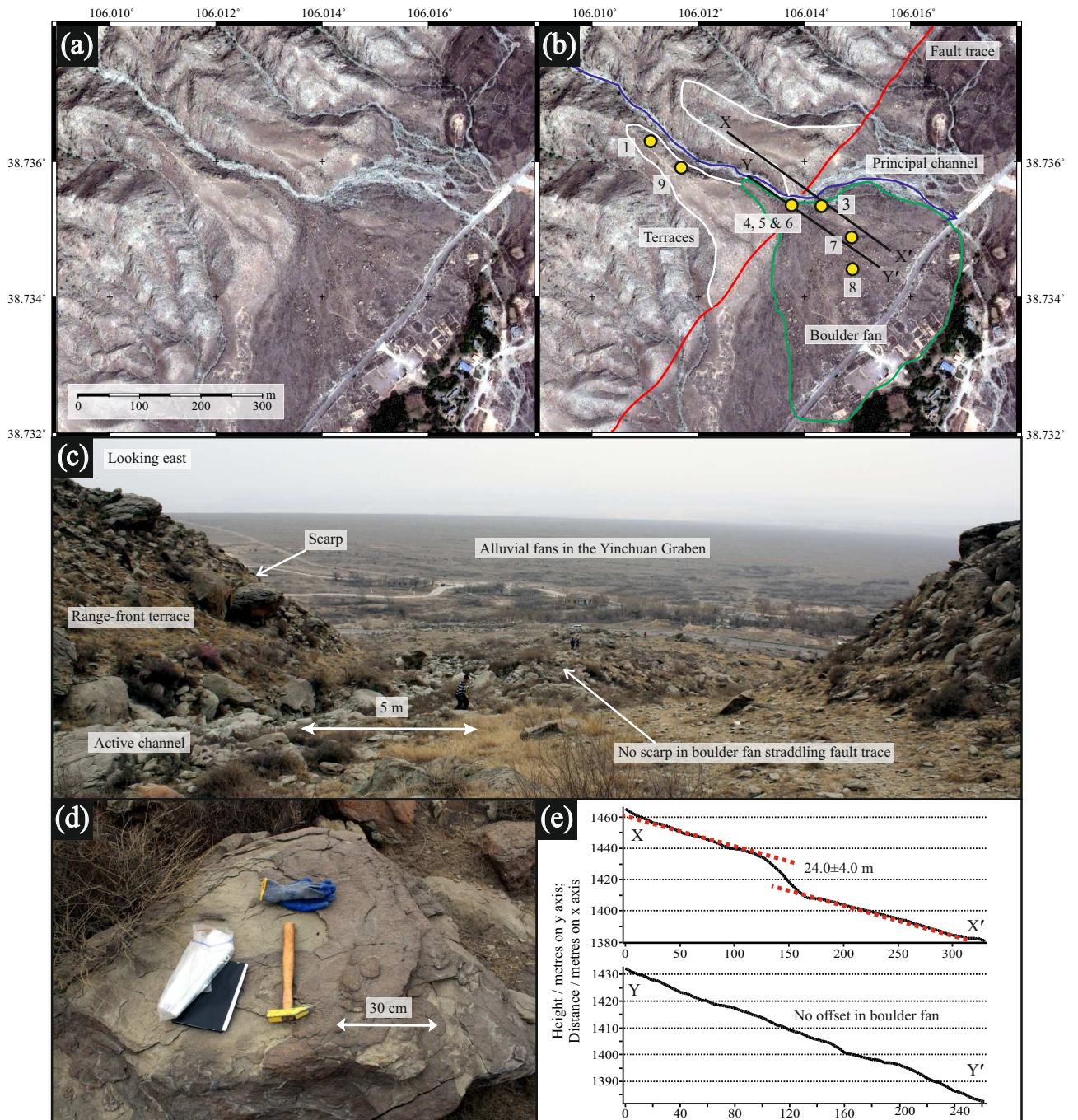


Figure 14. (a) Pleiades imagery of the range-front fault on the eastern flank of the Helanshan. (b) Annotated version of (a) showing fault trace (in red), two uplifted footwall terraces (in white), and an alluvial fan that has been deposited on top of the fault (in green). Yellow circles mark locations where boulder tops were collected for ^{10}Be exposure dating. (c) Annotated field photograph (taken at 38.735°N , 106.014°E) looking from the footwall, across the range-front fault trace, towards the boulder fan in the hanging wall. (d) Field photograph (taken at 38.735°N , 106.014°E) showing desert varnish on the top of the boulder where sample 4 was collected. (e) Topographic profiles from the Pleiades DEM along the lines marked X-X' and Y-Y' in (b).

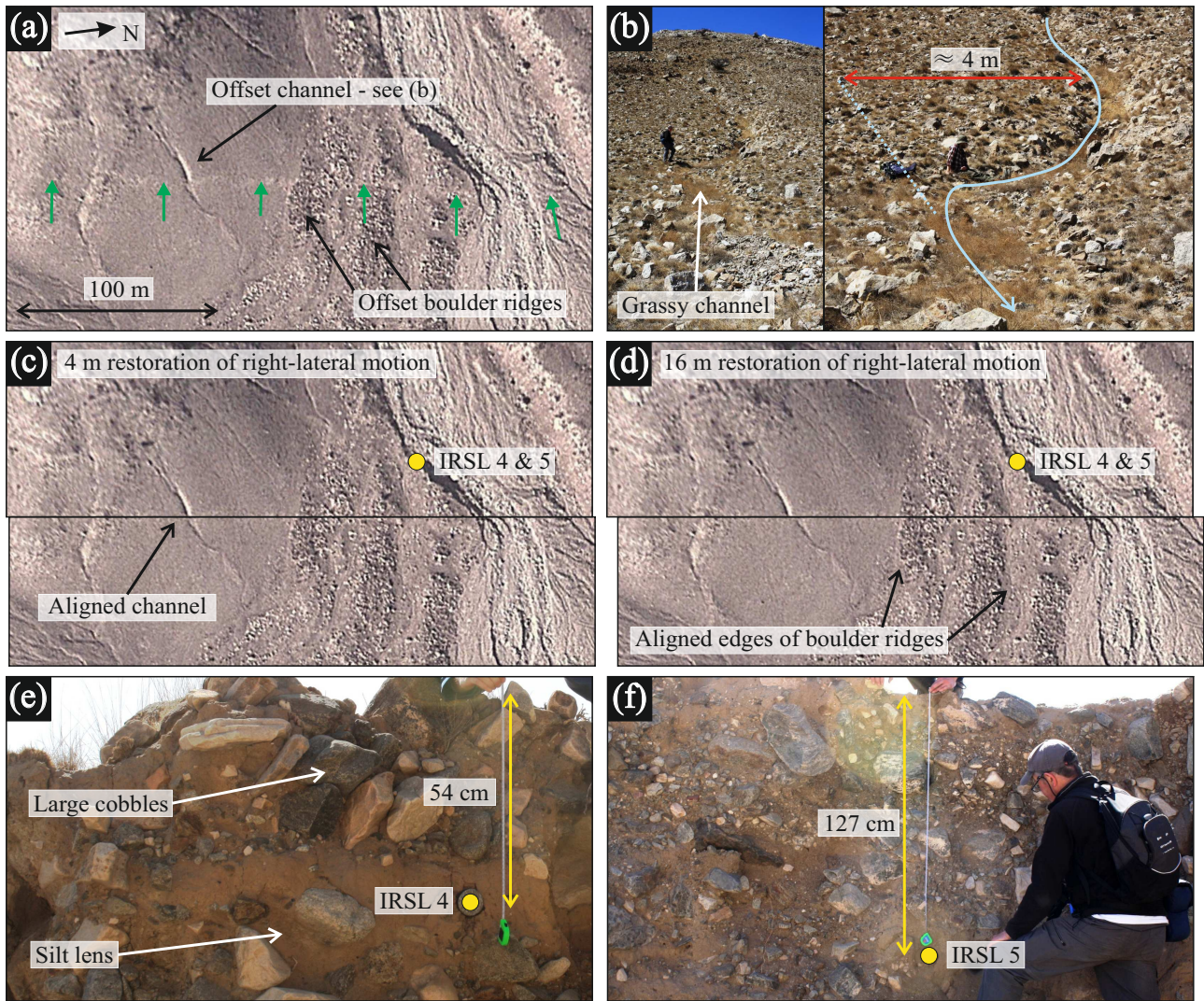


Figure 15. (a) Google Earth imagery from November 2011 (source: <http://earth.google.com>) of the northern end of the East Helanshan Fault, 10 km west of Huinong city. Fault scarp marked by green arrows and small offset visible in edges of boulder ridges. (b) Field photographs (taken at 39.235°N, 106.658°E, at the location marked in (a)). People for scale. The grassy channel records a right-lateral offset of approximately 4 m. (c) Same as (a) with a 4 m restoration of the right-lateral motion, which aligns the small channel shown in (b). Yellow circle indicates the location of IRSL samples 4 and 5. (d) Same as (a) with a 16 m restoration of the right-lateral motion, which aligns the edges of the boulder ridges as shown. Yellow circle indicates the location of IRSL samples 4 and 5. (e) Field photograph (taken at 39.236°N, 106.658°E) showing the sedimentary context of IRSL sample 4. (f) Field photograph (from the same location) showing the sedimentary context of IRSL sample 5.

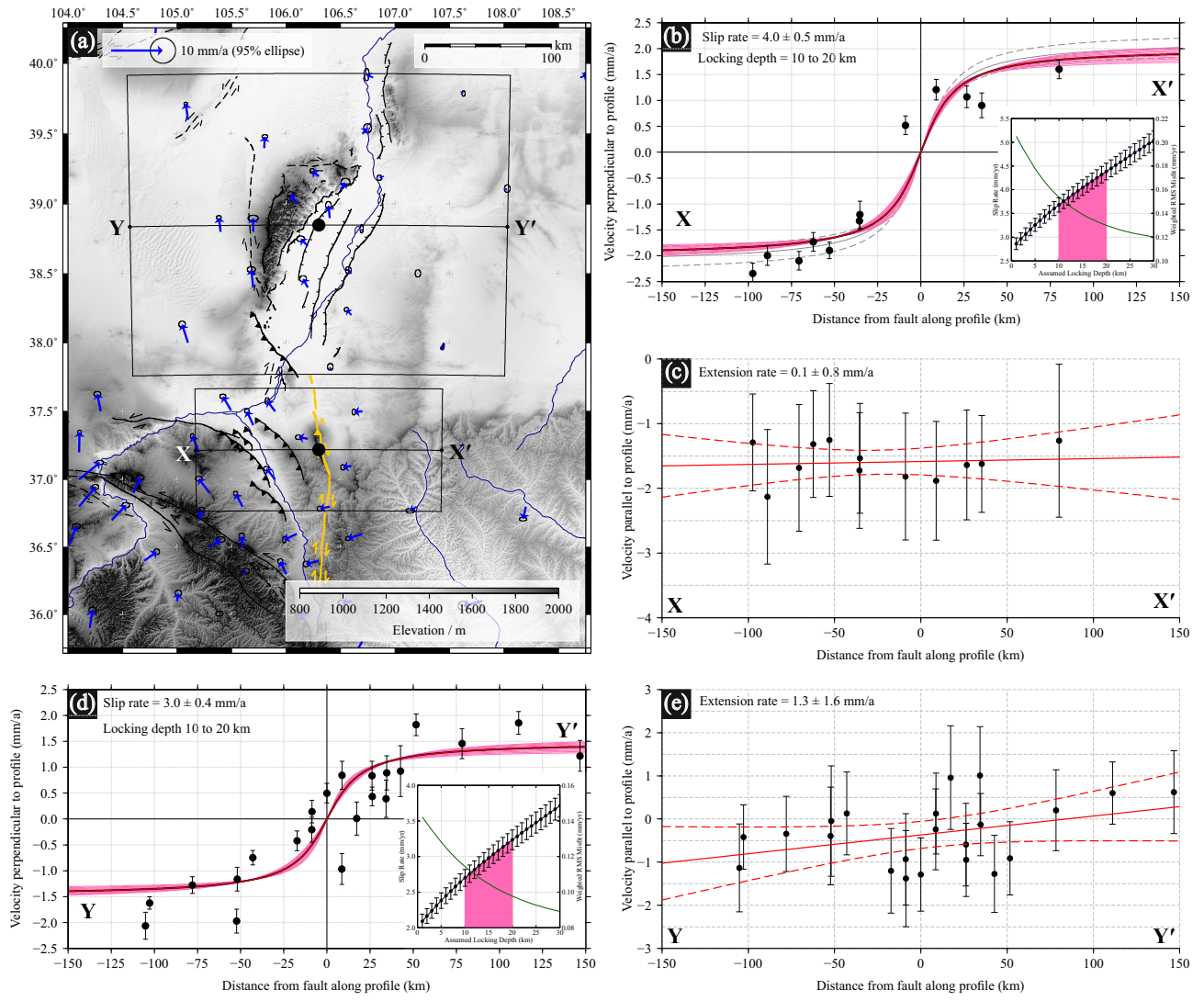


Figure 16. (a) SRTM topography (30 m resolution) of the western Ordos region, Ningxia Province, northern China [Farr *et al.*, 2007]. The Luoshan Fault and Yunwushan Fault are marked in orange. Blue vectors show campaign GPS measurements made over a period of 4 years (occupations in 2009, 2011 and 2013) [Zhao *et al.*, 2015] with a best fitting rigid body rotation (about an Euler pole at 46°N , 72°W , estimated from the vectors within this region) subtracted from all of the vectors. (b) Swath profile X-X' through the GPS data showing the component of velocity perpendicular to the profile azimuth of 90° . The red line shows the best fitting arctangent function ($u = \tan^{-1}\left(\frac{x}{d}\right)$, where u is the velocity, x is the distance from the fault and d is the locking depth). The dashed grey lines indicate the geologically determined slip rate on the Luoshan Fault of 4.3 ± 0.4 mm/a, assuming a locking depth of 15 km. The pink lines represent the range of best fitting solutions for assumed locking depths of between 10 and 20 km. The inset figure shows the trade-off between slip rate and locking depth. For this range of locking depths, we estimate a right-lateral slip rate of 4.0 ± 0.5 mm/a. (c) Swath profile X-X' showing the component of velocity parallel to the profile. The red lines show the best fit least squares regression to the data and the 95% confidence envelopes on this best fit line. No shortening or extension is resolvable within error along this profile. (d) Swath profile Y-Y' through the GPS data in the Yinchuan Graben showing the component of velocity perpendicular to the profile. Annotations as in (b). We estimate a right-lateral slip rate of 3.0 ± 0.4 mm/a. (e) Swath profile Y-Y' showing the component of velocity parallel to the profile. Annotations as in (c). We estimate an average extension rate across the whole profile of 1.3 ± 1.6 mm/a.

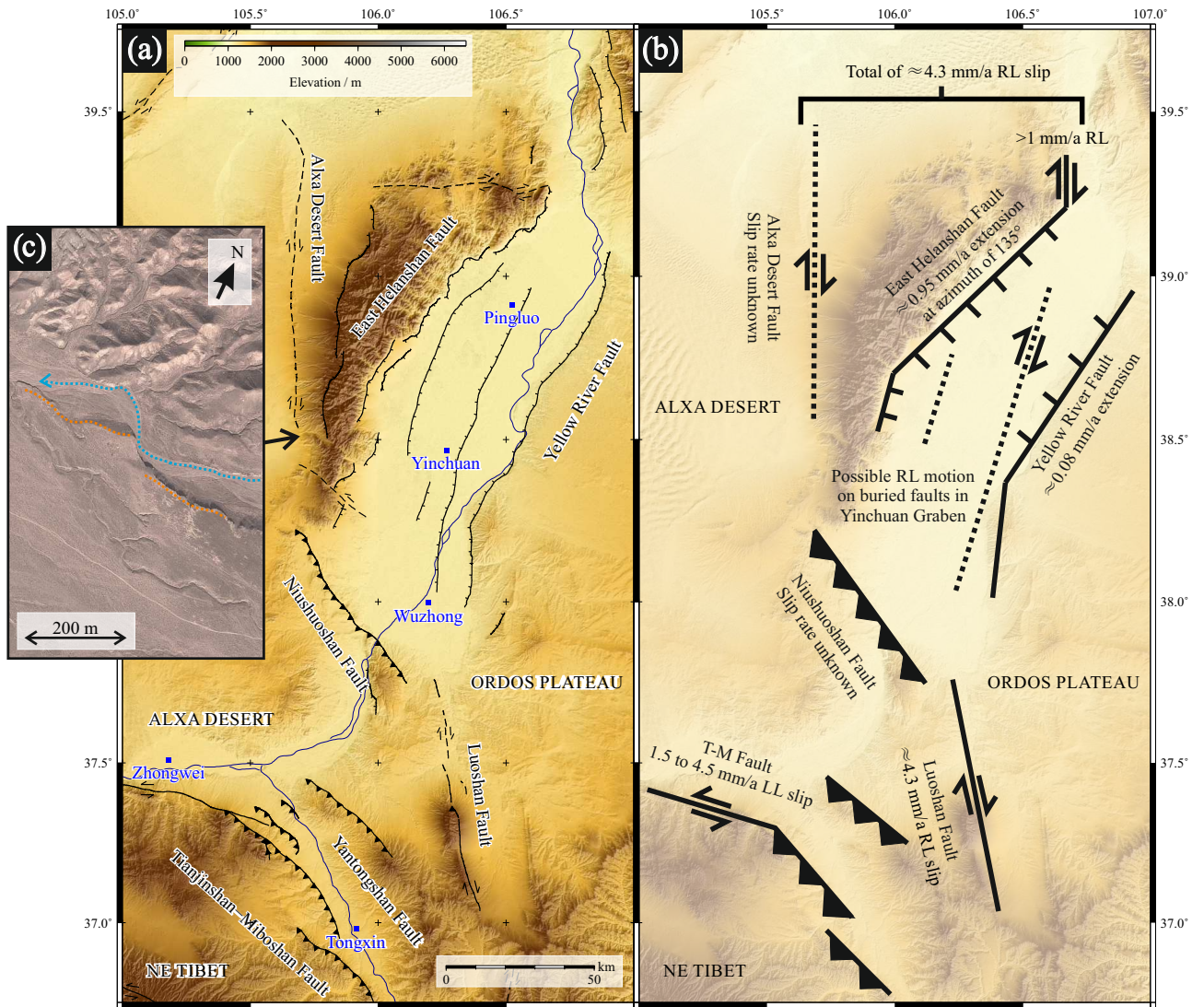


Figure 17. (a) SRTM topography (30 m resolution) of the western Ordos region in northern China [Farr *et al.*, 2007]. Cities are marked by blue squares and faults, marked as thin black lines, have been mapped from satellite imagery (source: <http://earth.google.com>) based upon earlier fault maps from Tapponnier and Molnar [1977], Deng *et al.* [1984], Zhang *et al.* [1990], Darby and Ritts [2002] and Darby *et al.* [2005]. (b) Geometric model for the tectonics of the western Ordos region showing the principal faults and their slip rates, from Zhang *et al.* [1990], Min *et al.* [2003], Deng *et al.* [2004] and this study. (c) Google Earth imagery from March 2011 (source: <http://earth.google.com>) showing right-lateral displacement of a channel (blue) and channel riser (orange) on the Alxa Desert Fault at 38.478°N , 105.721°E .

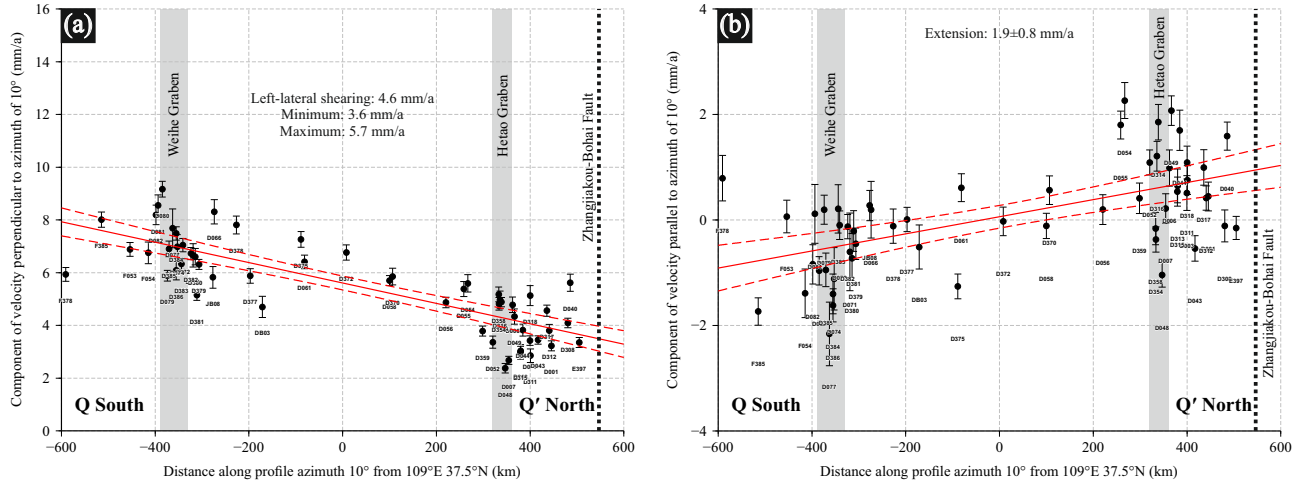


Figure 18. (a) Swath profile Q-Q' through the GPS data from *Zhao et al.* [2015] showing the velocity component perpendicular to the profile azimuth of 10° —same as Figure 2 (c). (See Figure 2 (a) for location.) The red line is the best fit least squares regression to the data and the dashed red lines are the 95% confidence envelopes on this best fit line. The profile shows left-lateral shearing of 4.6 ± 1.1 mm/a averaged over the extent of the profile. (b) Same as (a), but showing velocities parallel to an azimuth of 10° . The profile shows north-south extension of 1.9 ± 0.8 mm/a averaged over the extent of the profile.

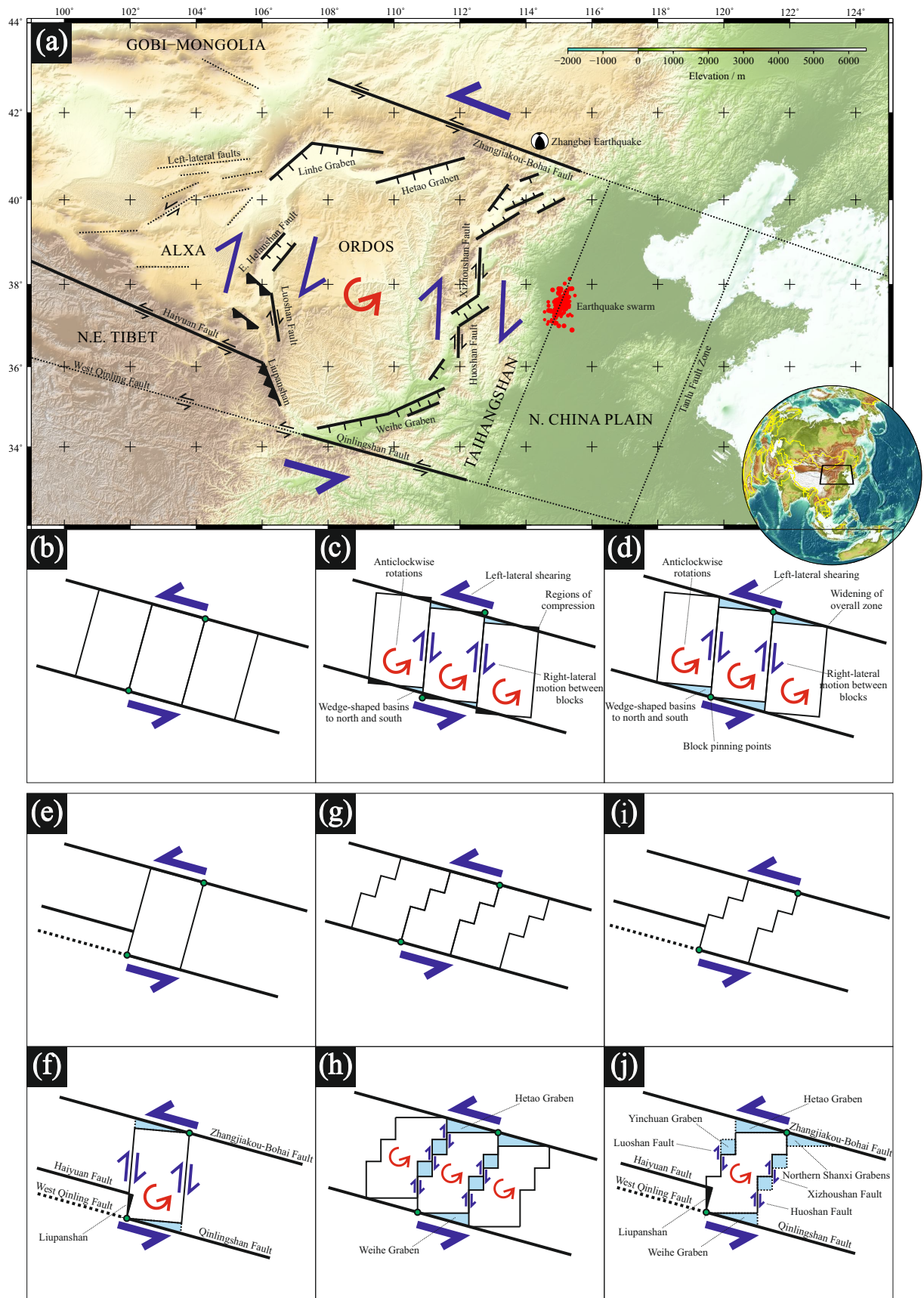


Figure 19. (a) SRTM topography of the Ordos Plateau in northeastern China [Farr *et al.*, 2007]. Inset globe shows the location of Figure 19 (a) within Asia. Black lines indicate major faults or fault zones and their sense of movement. Dotted lines show possible additional blocks—the Taihangshan and North China Plain blocks—to the east of the Ordos Plateau. General kinematic scheme after Xu and Ma [1992], Xu *et al.* [1993] and Xu *et al.* [1994]. (b), (c) and (d) Before and (two possible) after views showing a schematic kinematic representation of the anticlockwise rotation of three crustal blocks in a WNW-ESE left-lateral shear zone. (c) and (d) indicate that for the rotation to be accommodated, either compression must occur at the NE and SW corners of each block, or the overall zone has to widen. (e) and (f) Before and after views showing a more realistic geometry for the Haiyuan Fault and the resulting development of the Liupanshan. (g) and (h) Before and after views showing how corrugated block boundaries can lead to the development of en-echelon grabens with intervening right-lateral faults (e.g. the Luoshan, Huoshan and Xizhoushan Faults). (i) and (j) Before and after views combining the above modifications into a single schematic kinematic representation.